

Inkjet-Printed Graphene Electronics

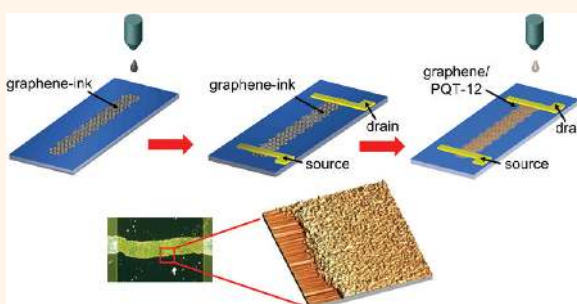
Felice Torrisi, Tawfique Hasan, Weiping Wu, Zhipei Sun, Antonio Lombardo, Tero S. Kulmala, Gen-Wen Hsieh, Sungjune Jung, Francesco Bonaccorso, Philip J. Paul, Daping Chu, and Andrea C. Ferrari*

Department of Engineering, University of Cambridge, Cambridge CB3 0FA, U.K.

Flexible electronics is a rapidly expanding research area.¹ Applications include touch screens,² electronic paper (e-paper),^{3,4} sensors,⁵ radio frequency tags,⁶ photovoltaic cells,^{7,8} light-emitting diodes,⁹ and electronic textiles.¹⁰ To date, it mainly relies on two fabrication strategies: one in which substrates bearing field-effect transistors (FETs) are bonded to plastic by transfer printing, or pick-and-place methods;¹¹ another in which FETs are prepared directly on the target substrate by several coating, curing, and lithographic steps.^{1,12} Rubber stamping,¹³ embossing,¹⁴ and inkjet printing^{15,16} reduce the number of such fabrication steps.

Inkjet printing is one of the most promising techniques for large-area fabrication of flexible plastic electronics.¹⁶ A range of components can be printed, such as transistors,^{14,16–19} photovoltaic devices,²⁰ organic light-emitting diodes (OLEDs),^{14,19,21} and displays.¹⁴ Inkjet printing is versatile,¹⁹ involves a limited number of process steps,²² is amenable for mass production, and can deposit controlled amounts of material.²² Drop on demand^{22,23} inkjet printing has progressed from printing text and graphics²² to a tool for rapid manufacturing,²⁴ being now a well-established technique to print thin-film transistors (TFTs) based on organic conducting and semiconducting inks.^{5,16,25} However, their mobilities, $\mu < 0.5 \text{ cm}^2 \text{ V}^{-1} \text{ s}^{-1}$,^{5,19} are still much lower than standard silicon technology. Several approaches aim to improve these results, such as the use of polysilicon,²⁶ zinc oxide nanoparticles,²⁷ and carbon nanotubes (CNTs).^{28–33} Metal nanoparticle inks are not stable in ordinary solvents, such as deionized (DI) water, acetone, isopropyl alcohol, *N*-methylpyrrolidone (NMP), or tetrahydrofuran.^{19,34} Therefore they need to be chemically modified in order to be dispersed¹⁹ via the use of stabilizers, which usually degrade in a couple of years.^{19,34} Metal nanoparticles also tend to oxidize after the printing process.^{19,34} Inkjet-printed CNT-TFTs have been reported with μ

ABSTRACT



We demonstrate inkjet printing as a viable method for large-area fabrication of graphene devices. We produce a graphene-based ink by liquid phase exfoliation of graphite in *N*-methylpyrrolidone. We use it to print thin-film transistors, with mobilities up to $\sim 95 \text{ cm}^2 \text{ V}^{-1} \text{ s}^{-1}$, as well as transparent and conductive patterns, with $\sim 80\%$ transmittance and $\sim 30 \text{ k}\Omega/\square$ sheet resistance. This paves the way to all-printed, flexible, and transparent graphene devices on arbitrary substrates.

KEYWORDS: graphene · inkjet printing · printed electronics · thin-film transistors

up to $50 \text{ cm}^2 \text{ V}^{-1} \text{ s}^{-1}$ and an ON/OFF ratio of $\sim 10^3$.³³

Graphene is the two-dimensional (2d) building block for sp^2 carbon allotropes of every other dimensionality. It can be stacked into 3d graphite, rolled into 1d nanotubes, or wrapped into 0d fullerenes.³⁵ It is at the center of an ever-expanding research area.^{35–38} Near-ballistic transport and high mobility make it an ideal material for nanoelectronics, especially for high-frequency applications.³⁹ Furthermore, its optical and mechanical properties are ideal for micro- and nanomechanical systems, thin-film transistors, transparent and conductive composites and electrodes, and photonics.^{35,38,40} Graphene was isolated by micromechanical exfoliation of graphite.⁴¹ This technique still gives the best samples in terms of purity, defects, mobility, and optoelectronic properties. However, large-scale production approaches are needed for widespread application. These encompass growth by chemical vapor deposition

* Address correspondence to acf26@eng.cam.ac.uk.

Received for review November 16, 2011 and accepted March 9, 2012.

Published online March 09, 2012
10.1021/nn2044609

© 2012 American Chemical Society

(CVD),^{42–47} sublimation of Si atoms by heat treatment of silicon carbide,^{48–51} segregation from metal substrates,^{52–55} and liquid phase exfoliation (LPE).^{56–59} Among these, LPE is ideally suited to produce printable inks.

Graphite can be exfoliated by chemical wet dispersion followed by ultrasonication, both in aqueous^{57,59} and nonaqueous solvents.^{56,59} Dispersions can be achieved by mild sonication of graphite in water with sodium deoxycholate, followed by sedimentation-based ultracentrifugation.^{59,60} Bile salt surfactants also allow the isolation of flakes with controlled thickness, when combined with density gradient ultracentrifugation.⁶¹ Exfoliation of graphite-intercalated compounds⁵⁸ and expandable graphite⁶² was also reported.

LPE was first achieved through sonication of graphite oxide,⁶³ following the Hummers method.⁶⁴ The oxidation of graphite in the presence of acids and oxidants^{65,66} disrupts the sp^2 network and introduces hydroxyl or epoxide groups,^{67,68} with carboxylic or carbonyl groups attached to the edge.^{67,68} These make graphene oxide (GO) sheets readily dispersible in water^{69,63} and several other solvents.⁷⁰ Although large GO flakes can be produced, these are intrinsically defective^{63,71} and electrically insulating.^{63,67} Despite several attempts,^{63,67} reduced GO (RGO) does not fully regain the pristine graphene electrical conductivity.^{72,67} It is thus important to distinguish between dispersion-processed graphene flakes,^{56–59} retaining the electronic properties of graphene, and insulating GO dispersions.^{63,72} Several groups reported GO-based inks.^{34,73,74} Reference 73 reported inkjet-printed RGO films for sensor applications, while ref 34 produced RGO-stabilized Cu nanoparticles as low-temperature metal colloids, to replace standard metal nanoparticle inks, which require high-temperature sintering post-processing.⁷⁵ Mobilities up to $90 \text{ cm}^2 \text{ V}^{-1} \text{ s}^{-1}$ have been achieved for highly reduced GO films by inkjet printing,⁷⁴ with an ON/OFF ratio up to 10.

Here we produce a graphene-based ink and demonstrate its viability for printed electronics.

RESULTS AND DISCUSSION

Ink Requirements. A key property of inks viable for printing is their ability to generate droplets.^{19,76} Ink viscosity, η [mPa s], surface tension, γ [mJ m^{-2}], density, ρ [g cm^{-3}], and nozzle diameter, a [μm], influence the spreading of the resulting liquid drops.⁷⁶ These can be arranged into dimensionless figures of merit (FOM), such as the Reynolds (Re),⁷⁷ Weber (We),⁷⁷ and Ohnesorge (Oh)⁷⁷ numbers: $\text{Re} = v\rho a/\eta$; $\text{We} = v^2\rho a/\gamma$, $\text{Oh} = (\text{We})^{1/2}/\text{Re} = -\eta/(\gamma\rho a)^{1/2}$, where v [m/s] is the drop velocity. During printing, the primary drop may be followed by secondary (satellite) droplets.^{23,78,79} This needs to be avoided in drop-on-demand printing.

Reference 80 suggested using $Z = 1/\text{Oh}$ as the FOM to characterize drop formation, $Z > 2$ being required to get single-drop ejection, with no satellite drops. In 2003, ref 76 surveyed commercial drop-on-demand systems, noting that they worked in the range $1 < Z < 10$. More recently, ref 79 experimentally confined Z between 4 and 14 by considering characteristics such as single-drop formability, position accuracy, and maximum allowable jetting frequency. However, several groups reported stable inkjet printing (*i.e.*, without satellite droplets) even for $Z > 14$ and $2 < Z < 4$. For example ref 81 demonstrated stable printing with $Z = 35.5$ for an ethylene glycol (EG)–water ink, ref 23 with $Z = 68.5$ for a glycerol–water, ref 82 with Z from 21 to 91 for polystyrene nanoparticle inks, whereas refs 83 and 84 with Z as low as 2.7 and 1 for glycerol–water and photoresist inks, respectively. By varying η , γ , and ρ we will tune Z across and outside the conventionally assumed optimal range ($1 < Z < 14$) in order to optimize our ink for drop-on-demand printing.

When inks contain dispersed molecules or nanoparticles, the latter should be smaller than the nozzle diameter, to prevent clogging.^{22,24} References 24 and 85 suggested, as a sufficient condition, that they should be at least $1/50$ of the nozzle diameter, in order to exclude any printing instability, such as clustering of the particles at the nozzle edge, which may cause deviation of the drop trajectory, or agglomerates, eventually blocking the nozzle. Here we use a nozzle diameter of $\sim 50 \mu\text{m}$; thus we aim for flake sizes less than $1 \mu\text{m}$ (this safe choice does not exclude the possibility that larger flakes, even $1/20$ of the nozzle size, could be printable).

The ejected drop behavior on the substrate can be described by fluid dynamics.⁸⁶ When a liquid droplet lands on a flat surface, partial wetting results in a finite angle between the liquid and the substrate,⁸⁶ known as the contact angle, θ_c .^{86–88} The drop size limit is given by^{78,79} $s[\mu\text{m}] = a[(\text{We} + 12)/(3(1 - \cos \theta_c) + (4\text{We}/\text{Re}^{1/2}))^{1/2}]$. The distance from the substrate must be optimized to guarantee both homogeneous printing and the highest resolution, barring any unusual jetting conditions, such as perturbations from the surrounding environment and diversion of the drop trajectory.^{19,76,78} Furthermore, a substrate very close to the nozzle causes secondary drops to scatter off during the impact of the primary drop,^{19,89} due to the initial drop jetting pressure, thus affecting the homogeneity of the final printed features.⁸⁹ The final assembly of printed nanoparticle inks depends on the substrate surface energy (SE),^{22,24} as well as ink viscosity and surface tension.²²

When a drop of an ink containing dispersed particles evaporates on a surface, it commonly leaves a dense, ring-like deposit along its perimeter.^{22,24} This is the so-called “coffee ring effect”,⁹⁰ *i.e.*, a distortion of the drops during solvent drying due to the interplay of ink viscosity and solute transport *via* solvent motion (arising from surface tension interaction between

solvent and substrate).^{19,90} This is one of the most important phenomena affecting the homogeneity of inkjet-printed drops.^{19,90} In order to prevent this, it is necessary to “freeze” the drops’ geometry immediately after they form a homogeneous and continuous film on the substrate.¹⁹

We print on Si/SiO₂ (to probe the electrical properties of our ink) and borosilicate (Pyrex 7740-Polished Prime grade) glass substrates (to test the viability of our ink to print transparent and conductive patterns), both with a roughness $R_z < 15$ nm. Our aim is to obtain inkjet-printed drops on a substrate with homogeneous flakes and uniform morphology, *i.e.*, with roughness comparable to the substrate. We obtain this by varying the contact angle and optimizing the substrate wettability.

In order to reduce the coffee ring effect, we need a solvent with both boiling point (T_c [°C]) and heat of vaporization (V_c [kJ/mol]) higher than water^{19,76,90} and a substrate that promotes adhesion.⁹¹ Thus we use NMP as solvent for exfoliation of graphite for two main reasons. First, it has a higher boiling point (~ 202 °C)⁹² and heat of vaporization (54.5 kJ/mol)⁹² than water (~ 100 °C and ~ 40 kJ/mol). Second, NMP is ideal for high-yield, surfactant-free exfoliation of graphite.^{56,59} We then test several surface treatments to optimize substrate adhesion. After printing, NMP is removed by thermal annealing at 170 °C for 5 min.

Graphene-Based Printable Ink. We prepare the graphene-based printable ink as follows. Graphite flakes (NGS Naturgraphit) are ultrasonicated (Decon bath, 20W) in NMP for 9 h. The unexfoliated flakes are left to settle for 10 min after ultrasonication. The decanted dispersions are then ultracentrifuged using a TH-641 swinging bucket rotor in a Sorvall WX-100 ultracentrifuge at 10 000 rpm ($\sim 15000g$) for an hour and filtered to remove flakes > 1 μm , which might clog the nozzle. The resulting ink is characterized by optical absorption spectroscopy (OAS), high-resolution transmission electron microscopy (HRTEM), electron diffraction, and Raman spectroscopy (see Methods).

A Perkin-Elmer Lambda 950 spectrometer with 1 nm resolution is used for the OAS measurements. OAS can be used to estimate the concentration of graphene^{56,57,60} via the Beer–Lambert law, according to the relation $A = \alpha cl$, where A is the absorbance, l [m] is the light path length, c [g/L] is the concentration of dispersed graphitic material, and α [$\text{L g}^{-1} \text{m}^{-1}$] is the absorption coefficient. Figure 1 plots an OAS spectrum of graphene ink diluted to 10%, to avoid possible scattering losses at higher concentrations. The spectrum in Figure 1 is mostly featureless, as expected due to linear dispersion of the Dirac electrons,^{38,40,93–96} the peak in the UV region being a signature of the van Hove singularity in the graphene density of states.⁹⁴ From $\alpha \approx 1390 \text{ L g}^{-1} \text{m}^{-1}$ at 660 nm, as for refs 57 and 59, we estimate $c \approx 0.11 \pm 0.02$ g/L.

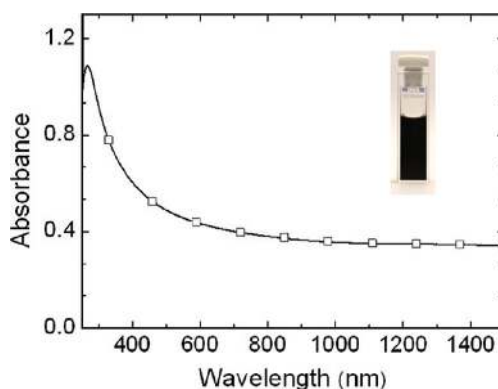


Figure 1. Absorbance of graphene ink diluted to 10%. Inset: a vial of undiluted ink.

Drops of inks are dispensed on holey carbon transmission electron microscopy (TEM) grids for TEM analysis, using a Tecnai T20 high-resolution electron microscope with an acceleration voltage of 200 kV operating in phase contrast mode. Figure 2a is a HRTEM image of a single-layer graphene (SLG) flake from the ink, while Figure 2b is a normal-incidence electron diffraction of the same flake as Figure 2a. It shows the expected 6-fold symmetry.^{97–99} The peaks are labeled with the corresponding Miller–Bravais (hkl) indexes. For few-layer graphene (FLG) flakes with Bernal (AB) stacking, the intensity ratio $I_{1100}/I_{2110} < 1$, while for SLG $I_{1010}/I_{2110} > 1$.^{97,99} We use this to distinguish SLG from FLGs.^{56,60} Figure 2c plots the diffraction intensity measured along the dashed line section through the $(1\bar{2}10)$, $(0\bar{1}10)$, $(\bar{1}010)$, and $(\bar{2}110)$ axis, reported in Figure 2b. The inner peaks, $(0\bar{1}10)$ and $(\bar{1}010)$, are ~ 1.5 times more intense than the outer ones, $(1\bar{2}10)$ and $(\bar{2}110)$, indicating that the flake is SLG.⁹⁷ The analysis of the edges also gives reliable information on the number of layers and can be used to investigate a large number of flakes,⁹⁷ from zoomed-in high-resolution edge images.^{56,100} If SLG folds or several SLGs stack one on the other, selected area diffraction is used to distinguish contentious cases.

These combined analyses show that our ink mostly consists of SLGs, bilayers (BLG), and FLGs, with lateral sizes of ~ 300 – 1000 nm. We find that $\sim 35\%$ SLGs are larger than 300 nm (Figure 2d); $\sim 40\%$ BLGs are larger than 350 nm (Figure 2e); $\sim 55\%$ FLGs are larger than 450 nm (Figure 2f). In particular, we have 33% SLG with $c \approx 0.11$ g/L. Previous works on LPE of graphene in NMP reported up to $\sim 28\%$ SLG for $c \approx 0.18$ g/L⁵⁹ and $\sim 21\%$ for $c \approx 1.8$ g/L.¹⁰⁰ Reference 58 also reported exfoliation of intercalated graphite in NMP, with $\sim 20\%$ SLGs for $c \approx 0.01$ g/L. Thus, our ink has higher SLG yield with respect to previous works, but lower c than ref 100. This higher c was achieved by long time (up to 460 h) ultrasonication.¹⁰⁰ However ref 100 reported defect formation and reduction of size as a result. Our combination of low-power ultrasonication (< 25 W) followed

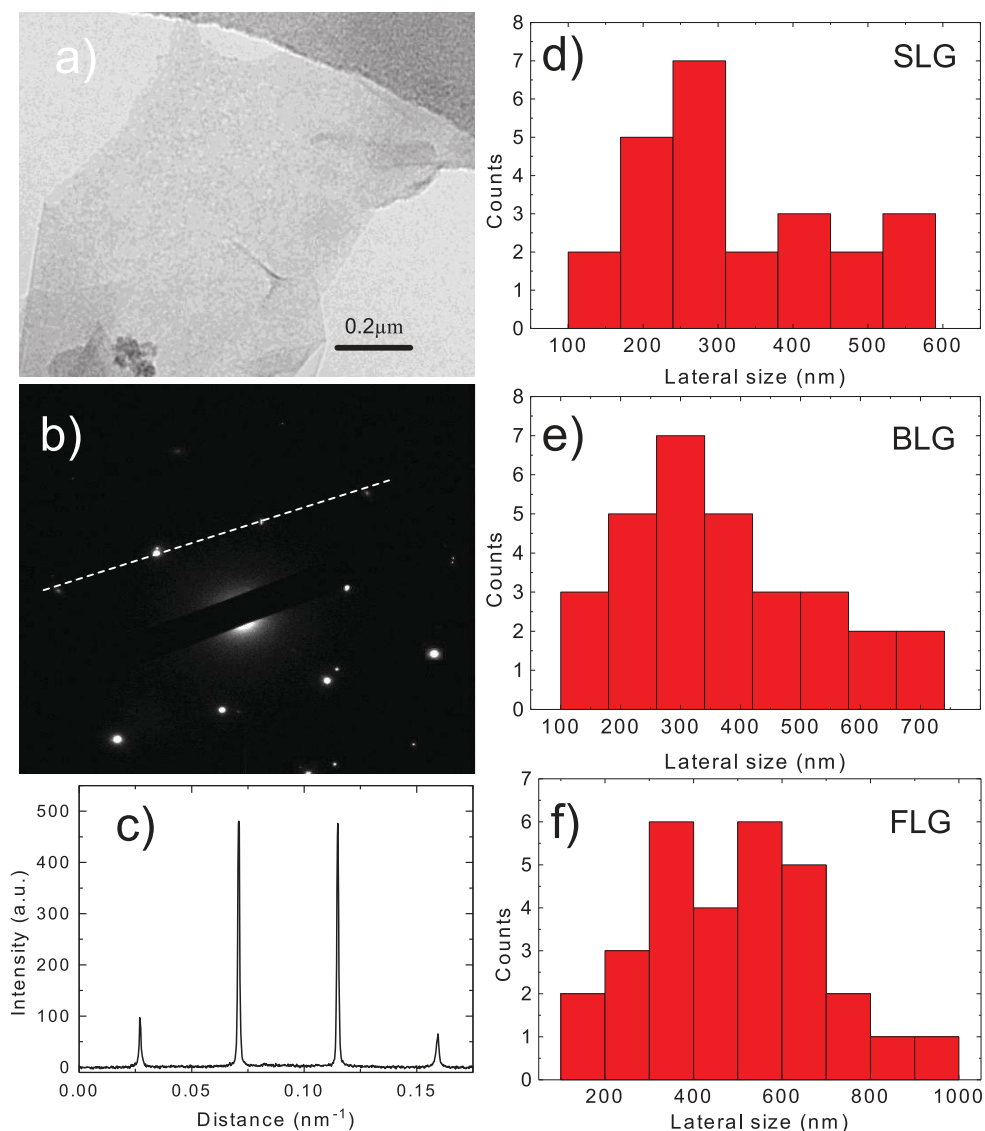


Figure 2. (a, b) HRTEM image and electron diffraction pattern of dispersion-cast SLG. (c) Diffracted intensity along the dashed line in b. Statistics of lateral size for (d) SLGs, (e) BLGs, and (f) FLGs.

by ultracentrifugation is ideal to obtain a high yield of defect-free SLGs.

Stable dispersions require the Gibbs free energy of mixing, ΔG_{mix} , to be zero or negative,¹⁰¹ where $\Delta G_{\text{mix}} = \Delta H_{\text{mix}} - K\Delta S_{\text{mix}}$, K being the temperature, ΔH_{mix} the enthalpy of mixing, and ΔS_{mix} the entropy change in the mixing process.^{56,101} For graphene and nanotubes, ΔS_{mix} is small.^{56,102} Therefore, for dispersion and stabilization of graphene in solvents, ΔH_{mix} needs to be very small. This can be achieved by choosing a solvent whose surface energy is very close to that of graphene.⁵⁶ The surface energy of NMP satisfies this requirement and allows efficient exfoliation of graphite. Graphite can also be efficiently exfoliated in water with the use of bile salt surfactants. Reference 103 reported $\sim 20\%$ SLGs for $c \approx 0.3$ g/L SLGs, while ref 60 reported $\sim 60\%$ SLGs for $c \approx 0.012$ g/L. The yield can be increased up to $\sim 80\%$ by density gradient

ultracentrifugation.⁶¹ The flake size of LPE graphene in water–surfactant dispersions is on average smaller (~ 200 nm,¹⁰³ ~ 30 nm⁶⁰) than thus far reported for NMP (~ 1 μm ^{59,56}). The viscosity of NMP at room temperature (1.7 mPa s)⁹² is higher than water (~ 1 mPa s).⁹² Larger flakes dispersed in a higher viscosity medium (such as NMP) experience higher frictional force^{104,105} and sedimentation coefficient,^{105,106} making it more difficult for them to sediment during ultracentrifugation. This reduces the SLG yield in NMP compared to water.

Figure 3a plots a typical Raman spectrum of the ink dispensed on Si/SiO₂ and annealed at 170 °C to remove NMP. Besides the G and 2D peaks, it shows significant D and D' intensities and the combination mode D + D' ≈ 2950 cm⁻¹. The G peak corresponds to the E_{2g} phonon at the Brillouin zone center. The D peak is due to the breathing modes of sp² rings and requires a defect for its activation by double resonance (DR).^{99,107,108} The 2D

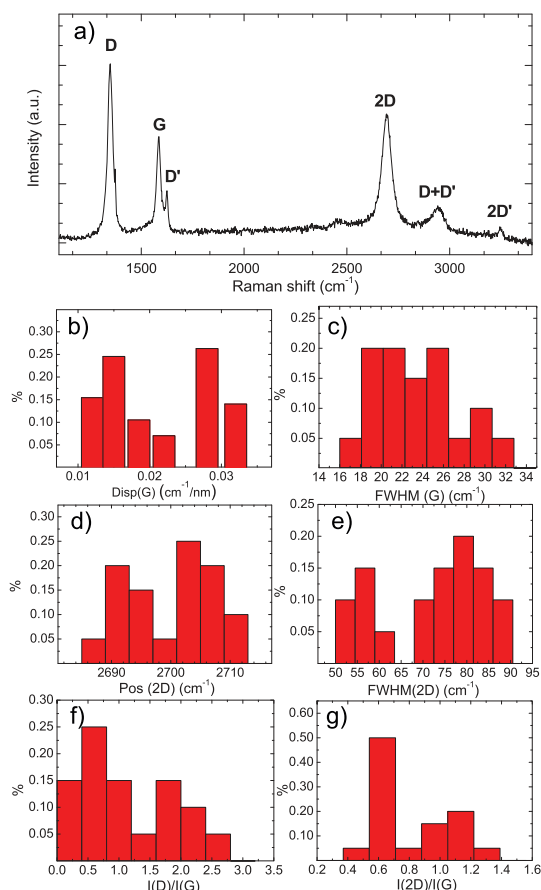


Figure 3. (a) Raman spectrum of graphene ink deposited on Si/SiO₂. Distribution of (b) Disp(G), (c) FWHM(G), (d) Pos(2D), (e) FWHM(2D), (f) $I(D)/I(G)$, and (g) $I(2D)/I(G)$ for 10 measurements.

peak is the second order of the D peak. This is a single band in SLG,⁹⁹ whereas it splits in four in BLG, reflecting the evolution of the band structure.⁹⁹ The 2D peak is always seen, even when no D peak is present, since no defects are required for the activation of two phonons from the other.⁹⁹ DR can also happen intravalley, *i.e.*, connecting two points belonging to the same cone around **K** or **K'**.^{107–109} This gives the D' peak. The 2D' is the second order of the D' peak.

We assign the D and D' peaks to the edges of the submicrometer flakes,¹¹⁰ rather than to the presence of a large amount of disorder within the flakes. This is further supported by the plot of the G peak dispersion, Disp(G) (Figure 3b) (see Methods). In disordered carbons the G peak position, Pos(G), increases as the excitation wavelength decreases, from IR to UV,¹⁰⁷ thus Disp(G) increases with disorder.^{111,107} The full width at half-maximum of the G peak, FWHM(G), always increases with disorder.^{113,112} Thus, combining the intensity ratio of the D and G peaks, $I(D)/I(G)$, with FWHM(G) and Disp(G) allows us to discriminate between disorder localized at the edges and disorder in the bulk of the samples. In the latter case, a higher $I(D)/I(G)$

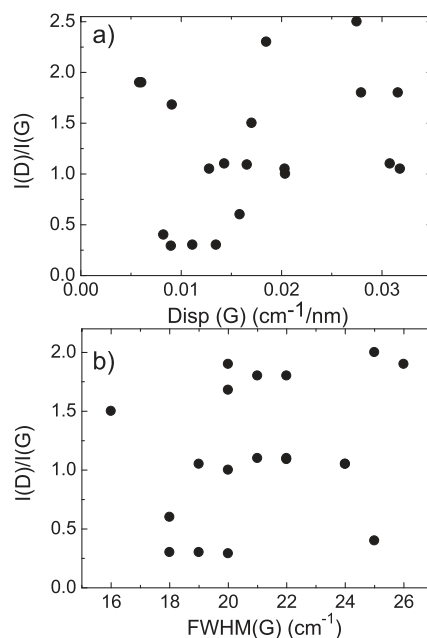


Figure 4. (a) $I(D)/I(G)$ as a function of Disp(G), (b) $I(D)/I(G)$ as a function of FWHM(G) measured on flakes deposited on Si/SiO₂.

would correspond to higher FWHM(G) and Disp(G). Figure 4 a,b show that Disp(G), $I(D)/I(G)$, and FWHM(G) are not correlated, a clear indication that the major contribution to the D peak comes from the sample edges. Also, Disp(G) is nearly zero for all samples, compared to the values larger than 0.1 cm⁻¹/nm expected for disordered carbons,^{111,114} another indication of the lack of large structural disorder within our flakes. The distribution of 2D peak position, Pos(2D), Figure 3d, has two maxima, ~2692 and 2705 cm⁻¹, similar to the FWHM(2D) distribution (Figure 3e). This is consistent with the samples being a distribution of SLG, BLG, and FLGs, but with a significant fraction of SLGs. We note that for the flakes with the smallest Pos(2D) and FWHM(2D), the ratio of the 2D and G integrated areas, $A(2D)/A(G)$, is at most 3.5, implying a doping of at least 10¹³ cm⁻².^{115–117}

We derive $\eta \approx 1.9$ mPa s from viscometer measurements and $\gamma \approx 40$ mJ m⁻² from tensiometer measurements. We estimate $\rho \approx 1.05$ g cm⁻³ by measuring with a micropipette (± 2 nL precision) the volume of 1 mg of ink [~ 0.952 mm³], at room temperature and pressure. Given these parameters, and our nozzle diameter of ~ 50 μ m, we get $Z \approx ((\gamma\rho a)^{1/2}/\eta) \approx 24$ for the graphene ink, in principle outside the conventionally assumed optimal range for printing.⁷⁹ We thus adjust η , ρ , and γ by mixing the ink with EG ($\eta \approx 20.5$ mPa s, $\gamma \approx 46$ mJ m⁻², $\rho \approx 1.09$ g cm⁻³) in order to bring Z within this range. We consider two mixtures: EG/graphene ink 20/80 ($\sim 80\%$ graphene ink; $\sim 20\%$ EG) and EG/graphene ink 80/20 ($\sim 20\%$ graphene ink; $\sim 80\%$ EG). We measure $\eta \approx 4.2$ mPa s, $\gamma \approx 42$ mJ m⁻², $\rho \approx 1.05$ g cm⁻³ for EG/graphene ink 20/80 and $\eta \approx 18$ mPa s, $\gamma \approx 46$ mJ m⁻²,

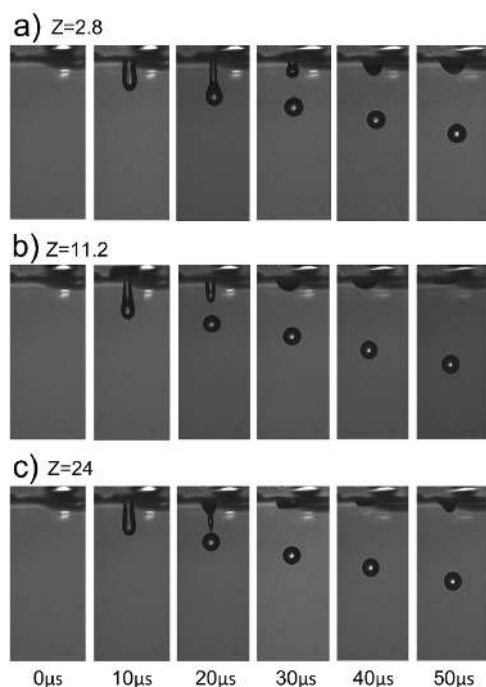


Figure 5. Drop formation in (a) EG/graphene ink 80/20 ($Z = 2.8$), (b) EG/graphene ink 20/80 ($Z = 11.2$), and (c) pristine graphene ink ($Z = 24$).

$\rho \approx 1.08 \text{ g cm}^{-3}$ for EG/graphene ink 80/20. This gives $Z \approx 11.2$ and ≈ 2.8 , both within the conventional range.^{76,79}

We use an Epson Stylus 1500 inkjet printer with a S020049 cartridge under a constant nitrogen flow. A high acquisition speed camera (Sony XCD-X700, with 10^5 s^{-1} acquisition rate) captures the dynamics of droplet formation. Shown in Figure 5a,b are drop ejection sequences for EG/graphene ink 80/20 and EG/graphene ink 20/80. These show individual drop ejection in both cases, as expected for inks within $1 < Z < 14$, with no satellite droplets. Figure 5c is the drop ejection sequence for the pristine graphene ink. Notably, even if $Z \approx 24$, we do not detect any satellite droplet. Hence, although Z is out of the conventionally assumed stable printing range,⁷⁹ Figure 5c shows that drop-on-demand from pristine graphene ink can be achieved. This shows that $1 < Z < 14$ is a sufficient, but not strictly necessary, condition for drop-on-demand printing. Thus, we will focus on the pristine graphene ink in the subsequent sections.

We note that LPE is a viable technique to achieve liquid dispersion of a range of layered materials (e.g., transition metal dichalcogenides, transition metal oxides, and other two-dimensional compounds such as BN, MoS_2 , Bi_2Te_3 , and Bi_2Se_3).¹¹⁸ Therefore, we envisage that our approach could be extended to provide a range of printable inks based on layered materials. These could then be mixed or printed to form hybrid heterostructures with novel properties.

Inkjet-Printed Features. The nozzle of our printer is $\sim 1 \text{ mm}$ above the substrate. The final layout of printed

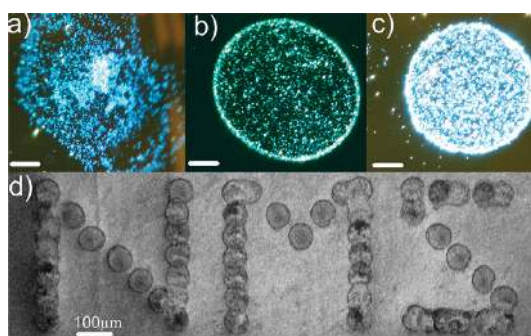


Figure 6. Dark-field optical micrograph of inkjet-printed drops on (a) plasma-cleaned, (b) pristine, and (c) HMDS-treated substrate. Scale is $20 \mu\text{m}$. (d) SEM micrograph of drops printed in a pattern.



Figure 7. Images of water drops dispensed on (a) O_2 -treated and (b) HMDS-treated Si/SiO_2 substrates.

nanoparticle inks depends on the substrate SE,^{22,24} as well as ink viscosity and surface tension.²² To investigate the influence of surface treatments, we print on pristine, hexamethyldisilazane (HMDS)-coated, and O_2 -plasma-treated Si/SiO_2 . HMDS is deposited by spin coating for 40 s at 1000 rpm, followed by annealing at 80°C for 2 min. The O_2 plasma is generated at 200 W and $4 \times 10^{-1} \text{ Torr}$ for 2 min. We use optical micrographs to visualize the inkjet-printed drops, Figure 6a,b,c. The bright green-blue color of the printed features is due to dark-field imaging. These reveal that HMDS constrains the drops to $\sim 90 \mu\text{m}$ diameter (Figure 6c), smaller than the other substrates (~ 100 and $\sim 150 \mu\text{m}$ for pristine, Figure 6b, and plasma-treated SiO_2 , Figure 6a). As discussed above, we use NMP as solvent to reduce the coffee ring effect compared to low boiling point solvents (e.g., water, chloroform).^{19,76,90} However, we still observe coffee rings when printing on pristine SiO_2 (Figure 6b), while Figure 6c reveals flake uniformity and no coffee rings on HMDS-treated SiO_2 . Thus, HMDS appears to prevent coffee rings. To understand this, we measure the substrates' SE and investigate the printed stripes' morphology, before and after surface treatment.

We utilize contact angle analysis to estimate the substrate surface tension, and SE. θ_c depends on the liquid surface tension^{86–88} and the substrate critical surface tension,^{86–88} according to Young's relation^{86,88,119} $\gamma_{\text{SV}} - \gamma_{\text{SL}} - \gamma_{\text{LV}} \cos \theta_c = 0$, where γ_{SV} [mJ m^{-2}] is the solid–vapor surface tension, γ_{SL} the solid–liquid surface tension, and γ_{LV} the liquid–vapor surface tension. Figure 6d is a representative printed pattern showing the viability of inkjet printing to fabricate complex layouts.

Figure 7a,b shows water drops printed onto O_2 and HMDS-treated Si/SiO_2 , with $\theta_c \approx 6^\circ$ and $\sim 65^\circ$,

indicating that the O₂-treated substrate SE is modified following HMDS treatment. γ_{LV} was measured as $\sim 73 \text{ mJ m}^{-2}$ in ref 120 for DI water, whereas $\gamma_{SV} \approx 116.5 \text{ mJ m}^{-2}$ and $\approx 40 \text{ mJ m}^{-2}$ were reported for O₂¹²¹ and HMDS-treated¹²² Si/SiO₂ substrates. Consequently, $\gamma_{SL} \approx 43.9 \text{ mJ m}^{-2}$ and $\sim 9.1 \text{ mJ m}^{-2}$ for O₂ and HMDS-treated Si/SiO₂. A higher γ_{SL} implies a higher SE.¹²³ Indeed, our γ_{SL} correspond to SEs ~ 73.9 and $\sim 39.1 \text{ mJ m}^{-2}$ for O₂ and HMDS-treated Si/SiO₂. A small θ_c results in the rapid drop spreading on the substrate,⁸⁶ as for O₂-treated SiO₂. HMDS provides higher θ_c , since it lowers γ_{SL} (thus the substrate SE), therefore reducing the wettability.^{87,124}

When inkjet printing stripes, the interdrop (*i.e.*, center-to-center) distance is an important parameter.¹²⁵ When the distance is large, individual drops are deposited.^{76,78,125} As the interdrop distance decreases, these merge into a line.¹²⁵ Thus, in order to obtain a continuous line, we need an interdrop distance smaller than the drop diameter.¹²⁵ On the other hand, refs 76 and 126 reported that a very small interdrop distance can result in particle aggregation on the substrate, thus a nonuniform stripe (*i.e.*, irregular edges). We select an interdrop distance suitable to have continuous lines, avoiding at the same time nonuniformities and irregular edges.

Shown in Figure 8a,b,c are optical images of printed stripes on pristine, O₂-plasma-treated and HMDS-treated Si/SiO₂, whereas Figure 8d,e,f plot the respective atomic force microscope (AFM) topographies. The stripe in Figure 8a is $\sim 100\text{--}110 \mu\text{m}$ wide, having an average thickness of $\sim 70 \text{ nm}$ and an irregular flake distribution, with aggregation of flakes. That in Figure 8b is wider ($\sim 130\text{--}140 \mu\text{m}$), with aggregates at the edges and an average thickness of $\sim 55 \text{ nm}$. The

stripe in Figure 8c has a more uniform and regular distribution of flakes, having a $\sim 85\text{--}90 \mu\text{m}$ width and $\sim 90 \text{ nm}$ average thickness. The width narrows going from the O₂-plasma-treated to the HMDS-treated Si/SiO₂, due to the SE decrease. Figure 8d,e show stripes with voids and irregular flake distribution, with $R_z \approx 30\text{--}40 \text{ nm}$. Figure 8f presents a more homogeneous network with $R_z \approx 15 \text{ nm}$. Thus, R_z is lower when θ_c is higher, because the poor wettability of drops with higher θ_c reduces the stripe width (as shown in Figure 8a,b,c), confining the flakes onto a smaller area. The uniformity of stripes printed on the HMDS-treated substrate corroborates the above considerations on the SE changes. In fact, the presence of silane groups in the molecular structure of HMDS⁹¹ acts as promoter of metallic particle adhesion to the substrate.^{91,127} Analogously, HMDS may promote the adhesion of graphene flakes to the substrate, thus favoring the formation of a regular network.

Figure 9a compares a typical Raman spectrum of a flake in the ink, with a measurement on the first stripe and on a stripe 90 nm thick, after 30 printing repetitions. Figure 9b,c,d,e,f,g and Figure 10 compare the Pos(2D), FWHM(2D), and Disp(G) distributions. The data show that the first stripe has very similar characteristics to the ink, as expected. However, the spectra after 90 repetitions show Pos(2D) and FWHM(2D) distributions more typical of a multilayer sample, having lost any direct signature of SLG. Note, however, that the 2D peak shape, even for the 90 nm stripe, remains distinctly different from that of graphite. A similar aggregation of flakes was previously observed for thick films derived from graphene dispersions.⁵⁶ In all cases Disp(G) remains similar and very low, again showing the lack of large amounts of defects within the flakes.

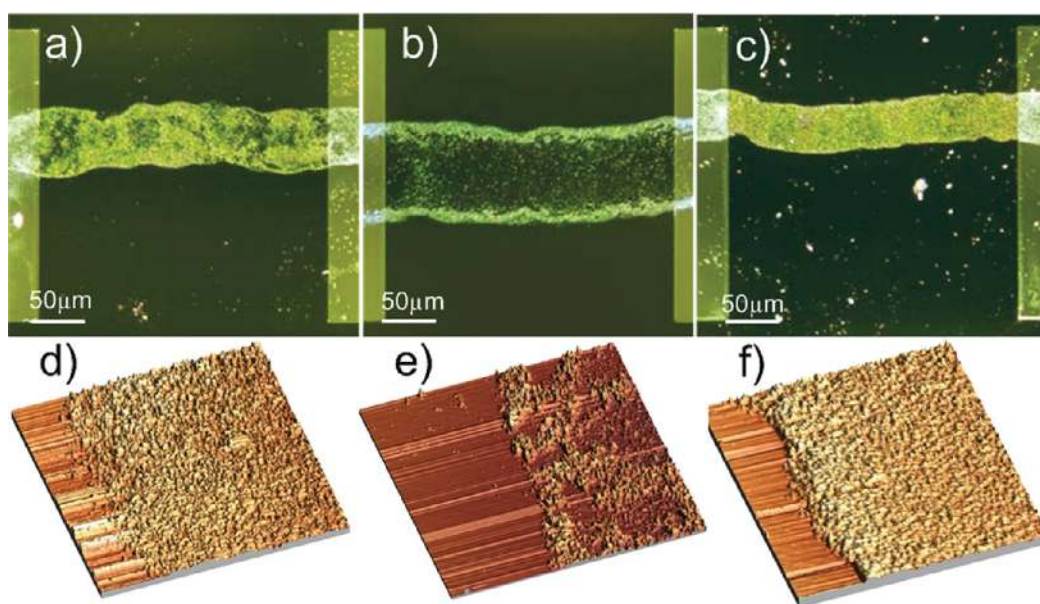


Figure 8. Optical micrograph of inkjet-printed stripes on (a) pristine, (b) O₂-treated and (c) HMDS-treated substrates. (d, e, f) AFM images of a, b, c, respectively.

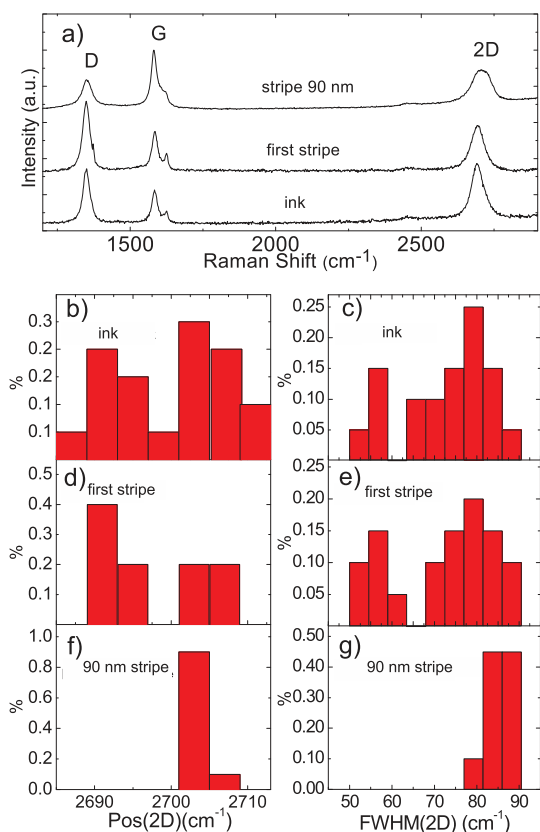


Figure 9. (a) Typical Raman spectrum of individual flakes in the ink, compared with spectra measured on the first stripe and on a stripe 90 nm thick. Pos(2D) and FWHM(2D) for (b, c) ink; (d, e) first stripe; and (f, g) 90 nm thick stripe.

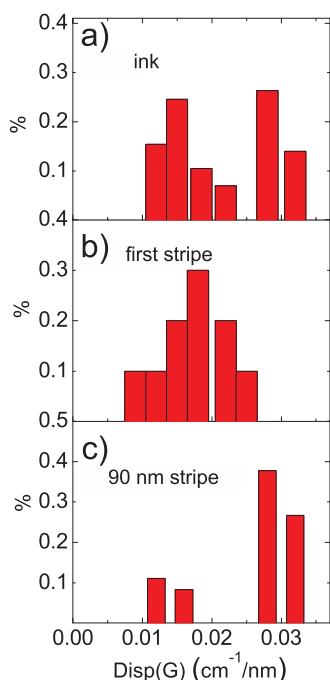


Figure 10. Distribution of Disp(G) for (a) ink; (b) first stripe; and (c) 90 nm thick stripe.

Transparent and Conductive Patterns. We now investigate the viability of our ink to print transparent and

conductive patterns. We characterize the sheet resistance R_s [Ω/\square] and transmittance T [%] of our stripes when placed on a transparent substrate. We thus use pristine and O_2 and HMDS-treated borosilicate glass, with $R_2 < 15$ nm, similar to SiO_2 on Si, but with $T \approx 99\%$ (Pyrex 7740-Polished Prime grade).

Figure 11a shows that for our stripes the thickness (t [nm]) increases linearly as a function of printing repetitions, with a slope defined by the surface treatment. Figure 11b plots the four-probe measured R_s (see Methods) as a function of t . For large t , R_s is ~ 34 , ~ 500 , and $\sim 10^5$ $k\Omega/\square$ for HMDS-treated, pristine, and O_2 -treated glass, respectively. For $t < 20$ nm, R_s increases for all substrates. For a thin film, $R_s = (\sigma t)^{-1}$, where σ [S/m] is the conductivity.¹²⁸ Thus, from Figure 11b and $\sigma = (R_s t)^{-1}$, we get the data in Figure 11c. σ is constant for $t > 20$ nm, in the case of HMDS-treated, pristine, and plasma-treated glass, with an average $\sigma \approx 10^2$, ~ 30 , and $\sim 10^{-1}$ S/m, respectively. Thus, stripes on HMDS-treated glass have a higher σ , combined with a more regular network of flakes, compared to the other two substrates. When $t < 20$ nm, σ decreases for all substrates. A similar trend was reported for CNT films on SiO_2 (produced by vacuum filtration),^{129,130} inkjet-printed CNT patterns on SiO_2 ,^{30,31} graphene films on SiO_2 ,^{131,132} and polyethylene-terephthalate,^{131,132} as well as Ag nanowire films, produced by vacuum filtration on SiO_2 .¹³¹ References 129–132 explained this decrease of σ for small t , due to percolation.

The percolation theory¹³³ predicts σ , for a network of conductive particles, to scale as¹³³

$$\sigma \propto (X - X_c)^\beta \quad (1)$$

where X [$\mu g/mm^2$] is the concentration of conductive particles per unit area, X_c [$\mu g/mm^2$] is the critical concentration of flakes corresponding to the percolation threshold, and β is the percolation exponent. Equation 1 can be rewritten in terms of t , rather than X , as¹²⁹

$$\sigma \propto (t - t_c)^\epsilon \quad (2)$$

where t_c is the critical thickness and ϵ is the percolation exponent. Figure 11c shows two regimes for σ as a function of t : a percolative linear behavior for $t < 20$ nm and a constant σ_{bulk} for $t > 20$ nm. Such regimes can be explained considering that our films stop behaving like bulk materials below a critical thickness (t_{min}), entering the percolation region.

The exponent ϵ can be estimated by a linear fit of the \log_{10} plot of σ vs t in the percolation region ($t < 20$ nm), Figure 12. We get $\epsilon \approx 4$ for stripes on HMDS-treated and pristine glass, while $\epsilon \approx 3$ for O_2 -treated glass. These values indicate percolation, as reported by refs 131 and 134–136 for networks with various geometries. ϵ is expected to increase with particle size^{135,136} and decrease with X_c .^{135,136} Assuming a

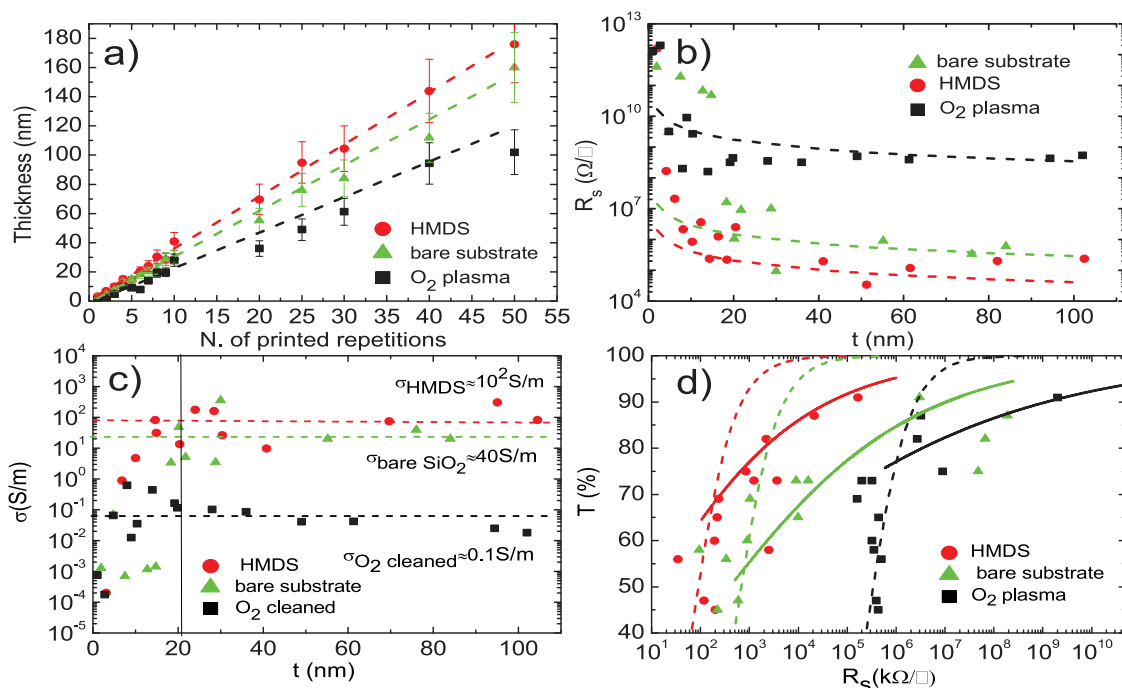


Figure 11. (a) Thickness as a function of printing repetitions. (b, c) R_s and σ as a function of thickness. (d) T as a function of R_s for HMDS-coated (red dots), O₂-plasma-treated (green triangles), and pristine (black squares) substrates.

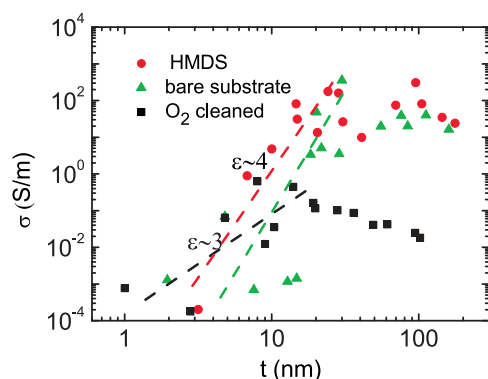


Figure 12. Conductivity as a function of film thickness, in logarithmic scale, for stripes printed on HMDS-treated (red dots), O₂-treated (green triangles), and pristine (black squares) substrates. Lines are fits in the percolation regime of conductivity.

similar particle size, since the same ink is used for all cases, we deduce that $\varepsilon \approx 4$ points to a larger X_c than $\varepsilon \approx 3$. This indicates formation of a more uniform network on HMDS-treated and pristine glass compared to O₂-treated glass.

We also determine the minimum concentration necessary to achieve the bulk conductivity regime. To do so, we assume $X \gg X_c$, because the bulk regime needs a tight network of interconnected flakes.^{131,134,137} Given our $c \approx 0.11 \text{ g/L}$, volume per printed drop of $\sim 10 \text{ nL}$,¹³⁸ and a dried drop size on the three substrates of ~ 90 , 100 , and $130 \mu\text{m}$, we estimate $X \approx 4 \times 10^{-2}$, $\sim 10^{-2}$, and $\sim 0.7 \times 10^{-2} \mu\text{g/mm}^2$ for stripes printed on HMDS, pristine, and plasma-treated glass, respectively. Consequently, from eq 1, σ for

stripes printed on HMDS-treated glass ($\sigma \approx 10^2 \text{ S/m}$) is higher than on pristine ($\sigma \approx 40 \text{ S/m}$) and plasma-treated glass ($\sigma \approx 0.1 \text{ S/m}$).

Figure 11d shows T as a function of R_s . The dashed lines are a plot of the relation $T = (1 + (Z_0 G_0) / (2R_s \sigma_{\text{bulk}}))^{-2}$ expected for graphene ink stripes with σ_{bulk} conductivity, where $Z_0 = 377 \Omega$ is the free-space impedance and $G_0 \approx 6 \times 10^{-5} \Omega^{-1}$ is the universal optical conductance of graphene.¹³⁹ The solid lines are a plot of $T = [1 + (1/\Pi)(Z_0/R_s)^{(1/\varepsilon+1)}]^{-2}$ expected for stripes in the percolative regime,¹³¹ where Π is the percolative figure of merit $\Pi = 2[(\sigma_{\text{bulk}}/G_0)/(Z_0 t_{\text{min}} G_0)]^{\varepsilon/(1/\varepsilon+1)}$. Our experimental T deviates from the dashed lines for $T > 75\%$. We assign this to the percolative regime, with σ_{DC} deviating from a bulk-like behavior. Also in this case, printing on HMDS-treated glass gives the highest T for a given R_s .

Inkjet-Printed Devices. Inkjet-printed TFTs based on organic semiconducting polymers have been widely investigated.^{16,140,141} The present state of the art devices^{140–142} have μ ranging from 0.01 to $\sim 0.5 \text{ cm}^2 \text{ V}^{-1} \text{ s}^{-1}$, with ON/OFF ratios up to 10^5 . Several inkjet-printed TFTs using various carbon nanomaterials have been reported. For example, fullerene-based TFTs were discussed in refs 143 and 144, with μ up to $0.01 \text{ cm}^2 \text{ V}^{-1} \text{ s}^{-1}$ and ON/OFF ratio of <10 . TFTs printed from CNT-based inks have been presented by several groups.^{28–30,32,33} The highest μ reported thus far is $\sim 50 \text{ cm}^2 \text{ V}^{-1} \text{ s}^{-1}$, combined with an ON/OFF ratio of 10^3 , but measured at 10^{-6} Torr .³³ Inkjet-printed TFTs from GO-based inks were discussed in refs 73 and 74, with μ up to $\sim 90 \text{ cm}^2 \text{ V}^{-1} \text{ s}^{-1}$ for an ON/OFF

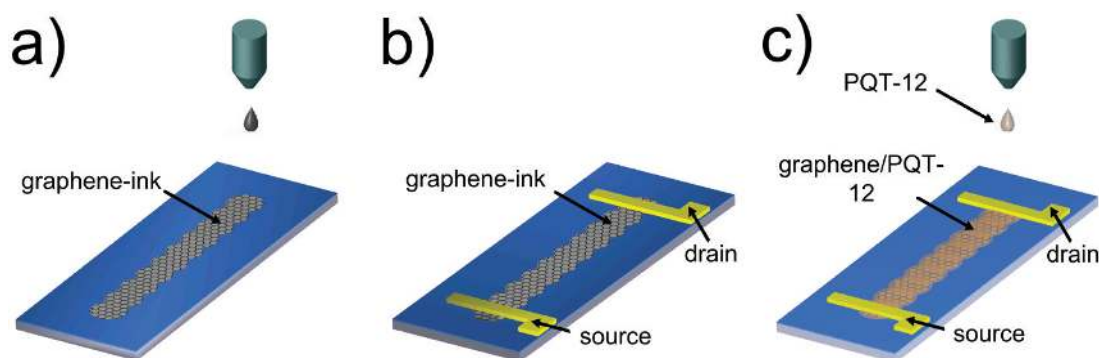


Figure 13. (a) Ink on Si/SiO₂. (b) Cr–Au pads define the source and drain contacts. (c) A layer of poly[5,5'-bis(3-dodecyl-2-thienyl)-2,2'-bithiophene] (PQT-12) is printed on top.

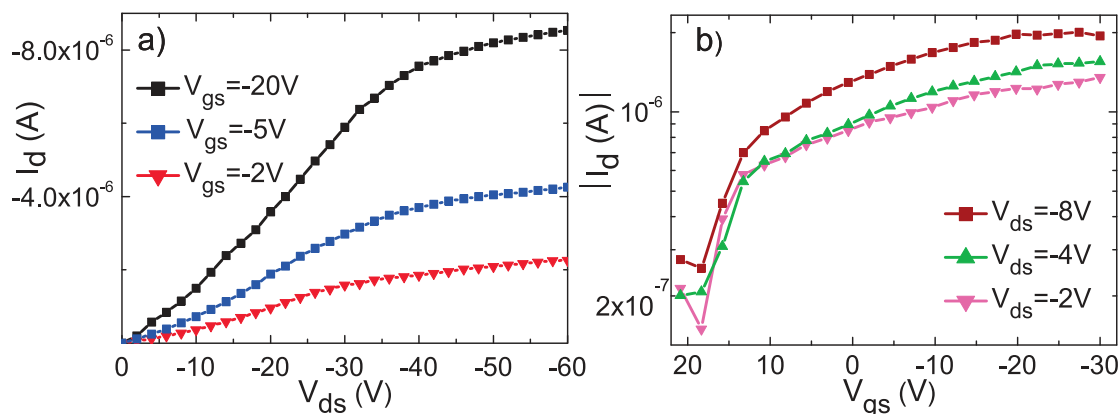


Figure 14. (a) Output and (b) transfer characteristics of an inkjet-printed graphene TFT.

ratio of 10 (measured at room conditions), after GO reduction.

We print graphene-TFTs as for Figure 13a and contact them with chromium–gold source and drain pads (Figure 13b). The output characteristics (shown in Figure 14a) are measured at $V_{gs} = -2, -5$, and -20 V, and transfer characteristics (shown in Figure 14b) are measured (at room conditions) at different drain voltages ($V_{ds} = -2, -4$, and -8 V). μ is derived from the slope of the transfer characteristic according to $\mu = (L/WC_i V_{ds})/(dI_d/dV_{gs})$, where L [μm] and W [μm] are the channel length and width, respectively, and C_i is the gate dielectric capacitance (~ 10 nF/cm²).¹⁴⁵ The geometry for all the printed TFTs is $L \approx 500$ μm , $W \approx 80$ μm , and thickness ≈ 25 nm.

We investigated how processing parameters such as interdrop distance, TFT channel thickness, surface treatment, and annealing temperature affect μ and ON/OFF ratio, in order to optimize the fabrication process for printed graphene-based TFTs. When varying the interdrop distance in a 25 nm thick graphene-TFT printed on a HMDS-treated substrate annealed at 170 °C, μ has a maximum for a ~ 40 μm interdrop (i.e. center-to-center) distance. This is consistent with the intuitive idea that optimized devices are obtained when the interdrop distance is roughly equal to the average drop diameter. When varying channel

thickness (for a graphene-TFT printed on a HMDS-treated substrate with a 40 μm interdrop distance, annealed at 170 °C), μ rapidly increases up to 95 cm² V⁻¹ s⁻¹ for a ~ 25 nm channel thickness, and then stays roughly constant, until decreasing for thicknesses larger than 40 nm. This behavior is expected, since we have shown in Figure 11 that percolation is reached for thicknesses > 20 nm. On the other hand, the field effect modulation becomes less effective when the channel is too thick. The post-annealing treatment improves mobilities and ON/OFF ratios with a plateau above 160 °C. However, we do not wish to increase too much the post-annealing temperature to avoid possible sample damage. We then considered how surface treatments of the substrate (O₂-plasma-treated, HMDS-treated, and pristine Si/SiO₂) affect μ and ON/OFF ratio for a 25 nm graphene-TFT, printed with a 40 μm interdrop distance and annealed at 170 °C. We obtain $\mu \approx 95$ cm² V⁻¹ s⁻¹ with an ON/OFF ratio of ~ 10 for the HMDS-treated substrate and worse performances for the other two substrates. This is yet again expected considering the coffee ring effects of non-optimized substrates, as shown in Figures 6 and 8.

We conclude that, in this particular experiment, the optimal processing parameters to inkjet print graphene-TFT correspond to an interdrop distance of ~ 40 μm , a channel thickness of ~ 25 nm, and an

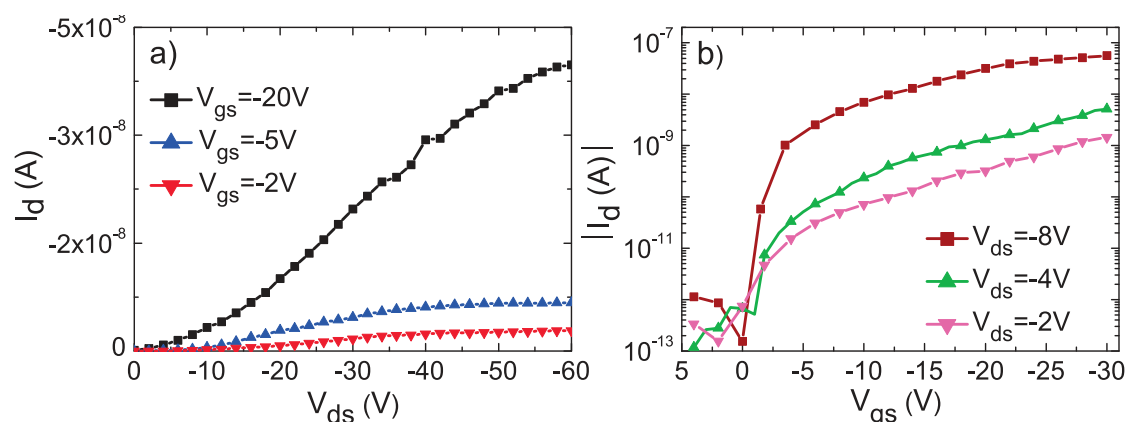


Figure 15. (a) Output and (b) transfer characteristics of an inkjet-printed graphene/PQT TFT.

annealing temperature of $\sim 170^\circ\text{C}$ on a substrate treated with HMDS. In this case $\mu \approx 95\text{ cm}^2\text{ V}^{-1}\text{ s}^{-1}$ and ON/OFF ratio ≈ 10 at $V_{\text{ds}} = -2\text{ V}$, comparable to those reported in ref 74 for inkjet-printed RGO TFTs. μ in our devices is almost 4 times higher than printed fullerene-based TFTs^{143,144} (for the same ON/OFF ratio ≈ 10) and more than 2 orders of magnitude higher than inkjet-printed CNTs^{28,30} (for the same ON/OFF ratio ≈ 10). However, the ON/OFF ratio in our TFTs is lower than the state of the art for CNTs (but measured at 10^{-6} Torr) at similar μ .³³ We note that inkjet-printed electronics requires high μ at room conditions.^{12,19} To date, CNT inkjet-printed devices measured at room conditions have μ no larger than $\sim 1\text{ cm}^2\text{ V}^{-1}\text{ s}^{-1}$ (at an ON/OFF ratio of ~ 10),³⁰ which is 2 orders of magnitude smaller than our inkjet-printed TFTs.

Organic semiconducting inks^{140–142} suffer from low μ , limited by variable range hopping of charges between isolated polymer chains.¹⁴⁶ The overall charge conduction in crystalline organic semiconducting thin films is determined by both intrachain and interchain charge transport.¹⁴⁷ The former is much faster than interchain hopping.^{146,147} Many groups tried to improve interchain hopping.^{28,29,148,149} Ref 148 proposed a chemical modification of a semiconducting organic ink by electron acceptors, while addition of Au nanoparticles was proposed in ref 149. Embedding CNTs in a semiconducting ink^{28,29} previously allowed us to get $\mu \approx 0.07\text{ cm}^2\text{ V}^{-1}\text{ s}^{-1}$ at room conditions.

We combine our graphene ink with one of the most common organic polymers in inkjet printing, poly[5,5'-bis(3-dodecyl-2-thienyl)-2,2'-bithiophene] (PQT-12),^{140–142} in order to investigate graphene's viability as an interchain hopping enhancer (similarly to Au nanoparticles and CNTs). PQT-12 is widely used

due to its higher environmental stability (up to 300 days at room conditions¹⁵⁰), with respect to other organic semiconducting inks.^{149,150}

We fabricate a graphene/PQT-12 TFT as shown in Figure 13a,b,c. Figure 15a plots its output characteristics at $V_{\text{gs}} = -2, -5$, and -20 V . For each V_{gs} , V_{ds} is swept from 0 to -60 V in steps of 2 V . At $V_{\text{ds}} = -8\text{ V}$, we get $\mu \approx 0.1\text{ cm}^2\text{ V}^{-1}\text{ s}^{-1}$ and an ON/OFF ratio of $\sim 4 \times 10^5$. The μ of graphene/PQT-12 TFT is about 10 times that of inkjet-printed CNTs/PQT-12 TFTs^{28,29} at an ON/OFF ratio of $\sim 10^5$. Compared to organic semiconducting polymers, our μ is 10 times that of inkjet-printed PQT-12^{141,142} and twice the highest reported value for inkjet-printed TFTs made of pure poly(2,5-bis(3-tetradecylthiophen-2-yl)thieno[3,2-b]thiophene).^{19,149,151,152} Thus, the combination of graphene and organic semiconducting inks is promising for high-performance printed electronics.

CONCLUSIONS

We demonstrated inkjet printing of graphene. Liquid phase exfoliated graphene is an ideal and low-cost material to make printable inks. Our graphene ink was used to print TFTs with μ up to $\sim 95\text{ cm}^2\text{ V}^{-1}\text{ s}^{-1}$. It was also combined with PQT-12 to fabricate devices with $\mu \approx 0.1\text{ cm}^2\text{ V}^{-1}\text{ s}^{-1}$ and ON/OFF ratios $\sim 4 \times 10^5$. This demonstrates its viability for flexible and transparent electronics. Our ink preparation technique can be generalized to a wide range of layered materials (*e.g.*, transition metal dichalcogenides, transition metal oxides, and other two-dimensional compounds such as BN, MoS_2 , Bi_2Te_3 , and Bi_2Se_3) that can also undergo liquid phase exfoliation. These could then be mixed or printed to form hybrid heterostructures with novel properties.

METHODS

Raman Spectroscopy. The ultracentrifuged dispersions are diluted and drop-cast onto a Si wafer with 300 nm thermally grown SiO_2 (LDB Technologies Ltd.). These samples are then

used for Raman measurements, collected with a Renishaw 1000 at 457 , 514.5 , and 633 nm and a $100\times$ objective, with an incident power of $\sim 1\text{ mW}$. The G peak dispersion is defined as $\text{Disp(G)} = \Delta\text{Pos(G)}/\Delta\lambda_L$, where λ_L is the laser excitation wavelength.

Disp(G) is generated from the linear fit of the Pos(G) plot as a function of the laser excitation wavelength.

Contact Angle and Surface Tension Measurements. A KSV CAM200 stage is used. The contact angle is measured by dispensing 1 μ L of ultrapure DI water on the substrates and measuring the angle at which the ink interface meets the solid surface. The surface tension is measured by the DuNouy–Padday technique.¹⁵³ This consists in using a rod of few millimeters in diameter, immersed in the dispersion and then pulled out. The rod is attached to a scale or balance via a thin metal hook that measures the maximum pull force. This is recorded as the probe is first immersed 1 mm into the solution and then slowly withdrawn.

Optical Transmittance. The transmittance is measured on samples that are inkjet printed on borosilicate glass (Pyrex 7740, Polished Prime grade) followed by annealing at 170 °C for 1 h, by scanning a 514.5 nm laser beam at 100 μ m steps. The transmitted beam is measured with a photodiode. An optical microscope equipped with 100 \times long-distance objective focuses the laser on the sample down to a spot size of \sim 2 μ m (incident power on the sample \sim 8 mW). The transmitted power intensity is measured by a Ophir Nova II power meter with 0.1 μ W resolution.

Electrical Measurements. Electrical measurements are performed using a Cascade AttoGuard probe station equipped with an Agilent 4156C semiconductor parameter analyzer. The integration time is set to 500 μ s and the delay time is set to 50 ms to ensure that no transient instabilities in the current occur.

Conflict of Interest: The authors declare no competing financial interest.

Acknowledgment. We acknowledge funding from ERC grant NANOPOTS, EPSRC grant EP/G030480/1, EU Grants RODIN and GENIUS, a Royal Society Wolfson Research Merit Award, the Cambridge Nokia Research Centre, The Royal Academy of Engineering, and King's College, Cambridge.

REFERENCES AND NOTES

- Cao, Q.; Kim, H.-S.; Pimparkar, N.; Kulkarni, J. P.; Wang, C.; Shim, M.; Roy, K.; Alam, M. A.; Rogers, J. A. Medium-Scale Carbon Nanotube Thin-Film Integrated Circuits on Flexible Plastic Substrates. *Nature* **2008**, *454*, 495–500.
- Zhou, L.; Wanga, A.; Wu, S.-C.; Sun, J.; Park, S.; Jackson, T. N. All-Organic Active Matrix Flexible Display. *Appl. Phys. Lett.* **2006**, *88*, 083502–083503.
- Ota, I.; Ohnishi, J.; Yoshiyama, M. Electrophoretic Image Display (EPID) Panel. *Proc. IEEE* **1973**, *61*, 832–836.
- Gelinck, G. H.; Huitema, H. E. A.; van Veenendaal, E.; Cantatore, E.; Schrijnemakers, L.; van der Putten, J. B. P. H.; Geuns, T. C. T.; Beenhakkers, M.; Giesbers, J. B.; Huisman, B. H.; *et al.* Flexible Active-Matrix Displays and Shift Registers Based on Solution-Processed Organic Transistors. *Nat. Mater.* **2004**, *3*, 106–110.
- Sekitani, T.; Yokota, T.; Zschieschang, U.; Klauk, H.; Bauer, S.; Takeuchi, K.; Takamiya, M.; Sakurai, T.; Someya, T. Organic Nonvolatile Memory Transistors for Flexible Sensor Arrays. *Science* **2009**, *326*, 1516–1519.
- Myny, K.; Steudel, S.; Vicca, P.; Beenhakkers, M. J.; van Aerle, N. A. J. M.; Gelinck, G. H.; Genoe, J.; Dehaene, W.; Heremans, P. Plastic Circuits and Tags for 13.56 MHz Radio-Frequency Communication. *Solid State Electron.* **2009**, *53*, 1220–1226.
- Granqvist, C. G. Transparent Conductors as Solar Energy Materials: A Panoramic Review. *Sol. Energy Mater. Sol. Cells* **2007**, *91*, 1529–1598.
- Yoon, J.; Baca, A. J.; Park, S.-I.; Elvikis, P.; Geddes, J. B.; Li, L.; Kim, R. H.; Xiao, J.; Wang, S.; Kim, T.-H.; *et al.* Ultrathin Silicon Solar Microcells for Semitransparent, Mechanically Flexible and Microconcentrator Module Designs. *Nat. Mater.* **2008**, *7*, 907–915.
- Han, T. H.; Lee, Y.; Choi, M. R.; Woo, S. H.; Bae, S. H.; Hong, B. H.; Ahn, J. H.; Lee, T. W. Extremely Efficient Flexible Organic Light-Emitting Diodes with Modified Graphene Anode. *Nat. Photonics* **2012**, *6*, 105–110.
- Schmied, B.; Gunther, J.; Klatt, C.; Kober, H.; Raemaekers, E. STELLA—STretchable Electronics for Large Area Applications—a New Technology for Smart Textiles. *Smart Textiles* **2009**, *60*, 67–73.
- Kim, D.; Jong-Hyun, A.; Hoon-Sik, K.; Keon Jae, L.; Tae-Ho, K.; Chang-Jae, Y.; Nuzzo, R. G.; Rogers, J. A. Complementary Logic Gates and Ring Oscillators on Plastic Substrates by Use of Printed Ribbons of Single-Crystalline Silicon. *IEEE Electron Device Lett.* **2008**, *29*, 73–76.
- Singh, T. B.; Sariciftci, N. S. Progress in Plastic Electronics Devices. *Annu. Rev. Mater. Res.* **2006**, *36*, 199–230.
- Rogers, J. A.; Bao, Z.; Baldwin, K.; Dodabalapur, A.; Crone, B.; Raju, V. R.; Kuck, V.; Katz, H.; Amundson, K.; Ewing, J.; *et al.* Paper-like Electronic Displays: Large-Area Rubber-Stamped Plastic Sheets of Electronics and Microencapsulated Electrophoretic Inks. *Proc. Natl. Acad. Sci. U. S. A.* **2001**, *98*, 4835–4840.
- Forrest, S. R. The Path to Ubiquitous and Low-Cost Organic Electronic Appliances on Plastic. *Nature* **2004**, *428*, 911–918.
- Bao, Z.; Rogers, J. A.; Katz, H. E. Printable Organic and Polymeric Semiconducting Materials and Devices. *J. Mater. Chem.* **1999**, *9*, 1895–1904.
- Sirringhaus, H.; Kawase, T.; Friend, R. H.; Shimoda, T.; Inbasekaran, M.; Wu, W.; Woo, E. P. High-Resolution Inkjet Printing of All-Polymer Transistor Circuits. *Science* **2000**, *290*, 2123–2126.
- Sun, Y. G.; Menard, E.; Rogers, J. A.; Kim, H. S.; Kim, S.; Chen, G.; Adesida, I.; Dettmer, R.; Cortez, R.; Tewksbury, A. Gigahertz Operation in Flexible Transistors on Plastic Substrates. *Appl. Phys. Lett.* **2006**, *88*, 183509.
- McAlpine, M. C.; Friedman, R. S.; Lieber, C. M. High-Performance Nanowire Electronics and Photonics and Nanoscale Patterning on Flexible Plastic Substrates. *Proc. IEEE* **2005**, *93*, 1357–1363.
- Singh, M.; Haverinen, H. M.; Dhagat, P.; Jabbour, G. E. Inkjet Printing—Process and Its Applications. *Adv. Mater.* **2010**, *22*, 673–685.
- Peumans, P.; Uchida, S.; Forrest, S. R. Efficient Bulk Heterojunction Photovoltaic Cells Using Small-Molecular-Weight Organic Thin Films. *Nature* **2003**, *425*, 158–162.
- Servati, P.; Nathan, A. Functional Pixel Circuits for Elastic AMOLED Displays. *Proc. IEEE* **2005**, *93*, 1257–1264.
- DeGans, B. J.; Duineveld, P.; Schubert, U. Inkjet Printing of Polymers: State of the Art and Future Developments. *Adv. Mater.* **2004**, *16*, 203–213.
- Dong, H. M.; Carr, W. W.; Morris, J. F. An Experimental Study of Drop-On-Demand Drop Formation. *Phys. Fluids* **2006**, *18*, 072102.
- Van Osch, T. H. J.; Perelaer, J.; de Laat, A. W. M.; Schubert, U. S. Inkjet Printing of Narrow Conductive Tracks on Untreated Polymeric Substrates. *Adv. Mater.* **2008**, *20*, 343–345.
- Yoo, J. E.; Lee, K. S.; Garcia, A.; Tarver, J.; Gomez, E. D.; Baldwin, K.; Sun, Y.; Meng, H.; Nguyen, T.-Q.; Loo, Y.-L. Directly Patternable, Highly Conducting Polymers for Broad Applications in Organic Electronics. *Proc. Natl. Acad. Sci. U. S. A.* **2010**, *107*, 5712–5717.
- Shimoda, T.; Matsuki, Y.; Furusawa, M.; Aoki, T.; Yudasaka, I.; Tanaka, H.; Iwasawa, H.; Wang, D.; Miyasaka, M.; Takeuchi, Y. Solution-Processed Silicon Films and Transistors. *Nature* **2006**, *440*, 783–786.
- Noh, Y.-Y.; Cheng, X.; Sirringhaus, H.; Sohn, J. I.; Welland, M. E.; Kang, D. J. Ink-jet Printed ZnO Nanowire Field Effect Transistors. *Appl. Phys. Lett.* **2007**, *91*, 043109–3.
- Beecher, P.; Servati, P.; Rozhin, A.; Colli, A.; Scardaci, V.; Pisana, S.; Hasan, T.; Flewitt, A. J.; Robertson, J.; Hsieh, G. W.; *et al.* Ink-jet Printing of Carbon Nanotube Thin Film Transistors. *J. Appl. Phys.* **2007**, *102*, 043710.
- Hsieh, G. W.; Li, F. M.; Beecher, P.; Nathan, A.; Wu, Y. L.; Ong, B. S.; Milne, W. I. High Performance Nanocomposite Thin Film Transistors with Bilayer Carbon Nanotube-Polythiophene Active Channel by Ink-Jet Printing. *J. Appl. Phys.* **2009**, *106*, 123706.

30. Takenobu, T.; Miura, N.; Lu, S.-Y.; Okimoto, H.; Asano, T.; Shiraishi, M.; Iwasa, Y. A. Ink-Jet Printing of Single-Walled Carbon Nanotube Thin Film Transistor. *Appl. Phys. Express* **2009**, *2*, 025005.
31. Okimoto, H.; Takenobu, T.; Yanagi, K.; Miyata, Y.; Shimotani, H.; Kataura, H.; Iwasa, Y. Tunable Carbon Nanotube Thin-Film Transistors Produced Exclusively via Inkjet Printing. *Adv. Mater.* **2010**, *22*, 3981–3986.
32. Okimoto, H.; Takenobu, T.; Yanagi, K.; Miyata, Y.; Kataura, H.; Asano, T.; Iwasa, Y. Ink-Jet Printing of a Single-Walled Carbon Nanotube Thin Film Transistor. *Jpn. J. Appl. Phys.* **2009**, *48*, 025003.
33. Ha, M.; Xia, Y.; Green, A. A.; Zhang, W.; Renn, M. J.; Kim, C. H.; Hersam, M. C.; Frisbie, C. D. Printed, Sub-3V Digital Circuits on Plastic from Aqueous Carbon Nanotube Inks. *ACS Nano* **2010**, *4*, 4388–4395.
34. Luechinger, N.; Athanassiou, A. E. K.; Stark, W. J. Graphene-Stabilized Copper Nanoparticles as an Air-Stable Substitute for Silver and Gold in Low-Cost Ink-Jet Printable Electronics. *Nanotechnology* **2008**, *19*, 445201.
35. Geim, A. K.; Novoselov, K. S. The Rise of Graphene. *Nat. Mater.* **2007**, *6*, 183–191.
36. Novoselov, K. S.; Geim, A. K.; Morozov, S. V.; Jiang, D.; Zhang, Y.; Dubonos, S. V.; Grigorieva, I. V.; Firsov, A. A. Electric Field Effect in Atomically Thin Carbon Films. *Science* **2004**, *306*, 666–669.
37. Charlier, J. C.; Eklund, P. C.; Zhu, J.; Ferrari, A. C. Electron and Phonon Properties of Graphene: Their Relationship with Carbon Nanotubes. *Top. Appl. Phys.* **2008**, *111*, 673–709.
38. Bonaccorso, F.; Sun, Z.; Hasan, T.; Ferrari, A. C. Graphene Photonics and Optoelectronics. *Nat. Photonics* **2010**, *4*, 611–622.
39. Lin, Y.-M.; Dimitrakopoulos, C.; Jenkins, K. A.; Farmer, D. B.; Chiu, H.-Y.; Grill, A.; Avouris, P. 100-GHz Transistors from Wafer-Scale Epitaxial Graphene. *Science* **2010**, *327*, 662.
40. Sun, Z.; Hasan, T.; Torrisi, F.; Popa, D.; Privitera, G.; Wang, F.; Bonaccorso, F.; Basko, D. M.; Ferrari, A. C. Graphene Mode-Locked Ultrafast Laser. *ACS Nano* **2010**, *4*, 803–810.
41. Novoselov, K. S.; Jiang, D.; Schedin, F.; Booth, T. J.; Khotkevich, V. V.; Morozov, S. V.; Geim, A. K. Two-Dimensional Atomic Crystals. *Proc. Natl. Acad. Sci. U. S. A.* **2005**, *102*, 10451–10453.
42. Karu, A. E.; Beer, M. Pyrolytic Formation of Highly Crystalline Graphite Films. *J. Appl. Phys.* **1966**, *37*, 2179–2181.
43. Obratzsov, A. N.; Obratzsova, E. A.; Tyurnina, A. V.; Zolotukhin, A. A. Chemical Vapor Deposition of Thin Graphite Films of Nanometer Thickness. *Carbon* **2007**, *45*, 2017–2021.
44. Kim, K. S.; Zhao, Y.; Jang, H.; Lee, S. Y.; Kim, J. M.; Kim, K. S.; Ahn, J.-H.; Kim, P.; Choi, J.-Y.; Hong, B. H. Large-Scale Pattern Growth of Graphene Films for Stretchable Transparent Electrodes. *Nature* **2009**, *457*, 706–710.
45. Reina, A.; Jia, X.; Ho, J.; Nezich, D.; Son, H.; Bulovic, V.; Dresselhaus, M. S.; Kong, J. Large Area, Few-Layer Graphene Films on Arbitrary Substrates by Chemical Vapor Deposition. *Nano Lett.* **2009**, *9*, 30–35.
46. Li, X. S.; Cai, W. W.; An, J. H.; Kim, S.; Nah, J.; Yang, D. X.; Piner, R.; Velamakanni, A.; Jung, I.; Tutuc, E.; *et al.* Large-Area Synthesis of High-Quality and Uniform Graphene Films on Copper Foils. *Science* **2009**, *324*, 1312–1314.
47. Bae, S.; Kim, H.; Lee, Y.; Xu, X.; Park, J.-S.; Zheng, Y.; Balakrishnan, J.; Lei, T.; Ri Kim, H.; Song, Y. I.; *et al.* Roll-to-Roll Production of 30-inch Graphene Films for Transparent Electrodes. *Nat. Nanotechnol.* **2010**, *5*, 574–578.
48. Berger, C.; Song, Z.; Li, T.; Li, X.; Ogbazghi, A. Y.; Feng, R.; Dai, Z.; Marchenkov, A. N.; Conrad, E. H.; First, P. N.; *et al.* Ultrathin Epitaxial Graphite: 2D Electron Gas Properties and a Route toward Graphene-Based Nanoelectronics. *J. Phys. Chem. B* **2004**, *108*, 19912–19916.
49. Acheson, E. G. Production of Artificial Crystalline Carbonaceous Materials; Article of Carborundum and Process of the Manufacture Thereof Carborundum. U.S. Patent 615,648, 1896.
50. Badami, D. V. Graphitization of α -Silicon Carbide. *Nature* **1962**, *193*, 569–570.
51. Emtsev, K. V.; Bostwick, A.; Horn, K.; Jobst, J.; Kellogg, G. L.; Ley, L.; McChesney, J. L.; Ohta, T.; Reshanov, S. A.; Rohrl, J.; *et al.* Towards Wafer-size Graphene Layers by Atmospheric Pressure Graphitization of Silicon Carbide. *Nat. Mater.* **2009**, *8*, 203–207.
52. Oshima, C.; Nagashima, A. Ultra-thin Epitaxial Films of Graphite and Hexagonal Boron Nitride on Solid Surfaces. *J. Phys.: Condens. Matter* **1997**, *9*, 1–20.
53. Gamo, Y.; Nagashima, A.; Wakabayashi, M.; Terai, M.; Oshima, C. Atomic Structure of Monolayer Graphite Formed on Ni(111). *Surf. Sci.* **1997**, *374*, 61–64.
54. Rosei, R.; De Crescenzi, M.; Sette, F.; Quaresima, C.; Savoia, A.; Perfetti, P. Structure of Graphitic Carbon on Ni(111): A Surface Extended-Energy-Loss Fine-Structure Study. *Phys. Rev. B* **1983**, *28*, 1161–1164.
55. Sutter, P. W.; Flege, J.-I.; Sutter, E. A. Epitaxial Graphene on Ruthenium. *Nat. Mater.* **2008**, *7*, 406–411.
56. Hernandez, Y.; Nicolosi, V.; Lotya, M.; Blighe, F. M.; Sun, Z.; De, S.; McGovern, I. T.; Holland, B.; Byrne, M.; Gun'ko, Y. K.; *et al.* High-Yield Production of Graphene by Liquid-Phase Exfoliation of Graphite. *Nat. Nanotechnol.* **2008**, *3*, 563–568.
57. Lotya, M.; Hernandez, Y.; King, P. J.; Smith, R. J.; Nicolosi, V.; Karlsson, L. S.; Blighe, F. M.; De, S.; Wang, Z.; McGovern, I. T.; *et al.* Liquid Phase Production of Graphene by Exfoliation of Graphite in Surfactant/Water Solutions. *J. Am. Chem. Soc.* **2009**, *131*, 3611–3620.
58. Valles, C.; Drummond, C.; Saadaoui, H.; Furtado, C. A.; He, M.; Roubeau, O.; Ortolani, L.; Monthieux, M.; Penicaud, A. Solutions of Negatively Charged Graphene Sheets and Ribbons. *J. Am. Chem. Soc.* **2008**, *130*, 15802–15804.
59. Hasan, T.; Torrisi, F.; Nicolosi, V.; Privitera, G.; Bonaccorso, F.; Ferrari, A. C. Solution-Phase Exfoliation of Graphite for Ultrafast Photonics. *Phys. Status Solidi B* **2010**, *247*, 2953.
60. Marago, O. M.; Bonaccorso, F.; Saija, R.; Privitera, G.; Gucciardi, P. G.; Lati, M. A.; Calogero, G.; Jones, P. H.; Borghese, F.; Denti, P.; *et al.* Brownian Motion of Graphene. *ACS Nano* **2010**, *4*, 7515–7523.
61. Green, A. A.; Hersam, M. C. Solution Phase Production of Graphene with Controlled Thickness via Density Differentiation. *Nano Lett.* **2009**, *9*, 4031–4036.
62. Li, X. L.; Wang, X. R.; Zhang, L.; Lee, S. W.; Dai, H. J. Chemically Derived, Ultrasoft Graphene Nanoribbon Semiconductors. *Science* **2008**, *319*, 1229–1232.
63. Stankovich, S.; Piner, R. D.; Nguyen, S. T.; Ruoff, R. S. Synthesis and Exfoliation of Isocyanate-Treated Graphene Oxide Nanoplatelets. *Carbon* **2006**, *44*, 3342–3347.
64. Hummers, W. S.; Offeman, R. E. Preparation of Graphitic Oxide. *J. Am. Chem. Soc.* **1958**, *80*, 1339–1339.
65. Brodie, B. C. Sur le Poids Atomique du Graphite. *Ann. Chim. Phys.* **1860**, *59*, 466–472.
66. Staudenmaier, L. Verfahren zur Darstellung der Graphitsäure. *Ber. Dtsch. Chem. Ges.* **1898**, *31*, 1481.
67. Mattevi, C.; Eda, G.; Agnoli, S.; Miller, S.; Mkhoyan, K. A.; Celik, O.; Mastrogianni, D.; Granozzi, G.; Garfunkel, E.; Chhowalla, M. Evolution of Electrical, Chemical, and Structural Properties of Transparent and Conducting Chemically Derived Graphene Thin Films. *Adv. Funct. Mater.* **2009**, *29*, 2577–2583.
68. Cai, W. W.; Piner, R. D.; Stadermann, F. J.; Park, S.; Shaibat, M. A.; Ishii, Y.; Yang, D. X.; Velamakanni, A.; An, S. J.; Stoller, M.; *et al.* Synthesis and Solid-State NMR Structural Characterization of C-13-Labeled Graphite Oxide. *Science* **2008**, *321*, 1815–1817.
69. Eda, G.; Chhowalla, M. Chemically Derived Graphene Oxide: Towards Large-Area Thin-Film Electronics and Optoelectronics. *Adv. Mater.* **2010**, *22*, 2392–2415.
70. Paredes, J. I.; Villar-Rodil, S.; Martinez-Alonso, A.; Tascon, J. M. D. Graphene Oxide Dispersions in Organic Solvents. *Langmuir* **2008**, *24*, 10560–10564.

71. He, H.; Klinowski, J.; Forster, M.; Lerf, A. A New Structural Model for Graphite Oxide. *Chem. Phys. Lett.* **1998**, *287*, 53–56.
72. Eda, G.; Fanchini, G.; Chhowalla, M. Large-Area Ultrathin Films of Reduced Graphene Oxide as a Transparent and Flexible Electronic Material. *Nat. Nanotechnol.* **2008**, *3*, 270–274.
73. Dua, V.; Surwade, S.; Ammu, S.; Agnihotra, S.; Jain, S.; Roberts, K.; Park, S.; Ruoff, R.; Manohar, S. All-Organic Vapor Sensor Using Inkjet-Printed Reduced Graphene Oxide. *Angew. Chem., Int. Ed.* **2010**, *49*, 2154–2157.
74. Wang, S.; Ang, P. K.; Wang, Z.; Tang, A. L. L.; Thong, J. T. L.; Loh, K. P. High Mobility, Printable, and Solution-Processed Graphene Electronics. *Nano Lett.* **2009**, *10*, 92–98.
75. Park, B. K.; Kim, D.; Jeong, S.; Moon, J.; Kim, J. S. Direct Writing of Copper Conductive Patterns by Ink-Jet Printing. *Thin Solid Films* **2007**, *515*, 7706–7711.
76. Derby, B.; Reis, N. Inkjet Printing of Highly Loaded Particulate Suspensions. *MRS Bull.* **2003**, *28*, 815.
77. Batchelor, G. K. In *An Introduction to Fluid Dynamics*; Cambridge University Press, 1967.
78. Reis, N.; Derby, B. Ink Jet Deposition of Ceramic Suspensions: Modelling and Experiments of Droplet formation. *MRS Symp. Proc.* **2000**, *624*, 65.
79. Jang, D.; Kim, D.; Moon, J. Influence of Fluid Physical Properties on Ink-Jet Printability. *Langmuir* **2009**, *25*, 2629–2635.
80. Fromm, J. E. Numerical-Calculation of the Fluid-Dynamics of Drop-on-Demand Jets. *IBM J. Res. Dev.* **1984**, *28*, 322.
81. Shin, P.; Sung, J.; Lee, M. H. Control of Droplet Formation for Low Viscosity Fluid by Double Waveforms Applied to a Piezoelectric Inkjet Nozzle. *Microelectron. Reliab.* **2011**, *51*, 797–804.
82. de Gans, B.; Kazancioglu, E.; Meyer, W.; Schubert, U. S. Inkjet Printing Polymers and Polymer Libraries Using Micropipettes. *Macromol. Rapid Commun.* **2004**, *25*, 292–296.
83. Jung, S.; Hutchings, I. M. The Impact and Spreading of a Small Liquid Drop on a Non-Porous Substrate Over an Extended Time Scale. *Soft Matter* **2012**, *8*, 2686–2696.
84. Hsiao, W. K.; Hoath, S. D.; Martin, G. D.; Hutchings, I. M. Ink Jet Printing for Direct Mask Deposition in Printed Circuit Board Fabrication. *J. Imaging Sci. Technol.* **2009**, *53*, 050304.
85. Fluid Properties Effects on Ink-Jet Device Performance, *MicroFab technote* 1999, online access: <http://www.microfab.com/equipment/technote/technote99-02.pdf>.
86. De Gennes, P. G. Wetting: Statics and Dynamics. *Rev. Mod. Phys.* **1985**, *57*, 827–863.
87. Shafirin, E. G.; Zisman, W. A. Constitutive Relations in the Wetting of Low Energy Surfaces and the Theory of the Retraction Method of Preparing Monolayers. *J. Phys. Chem.* **1960**, *64*, 519–524.
88. Israelachvili, J. In *Intermolecular and Surface Forces*; Academic Press: New York, 1991.
89. Park, J. S.; Kim, J. P.; Song, C.; Lee, M. Control of Inkjet Printed Profiles by Solvent-Vapor Annealing. *Displays* **2010**, *31*, 164–167.
90. Deegan, R. D.; Bakajin, O.; Dupont, T. F.; Huber, G.; Nagel, S. R.; Witten, T. A. Capillary Flow as the Cause of Ring Stains from Dried Liquid Drops. *Nature* **1997**, *389*, 827–829.
91. Osthoff, R. C.; Kantor, S. W. *Organosilazane Compounds*; John Wiley & Sons, Inc.: New York, 1997.
92. Lide, D. R. In *Handbook of Chemistry and Physics*, 86th ed.; CRC Press Inc.: Boca Raton, FL, 2005.
93. Mak, K. F.; Sfeir, M. Y.; Wu, Y.; Lui, C. H.; Misewich, J. A.; Heinz, T. F. Measurement of the Optical Conductivity of Graphene. *Phys. Rev. Lett.* **2008**, *101*, 196405.
94. Kravets, A.; Grigorenko, N.; Nair, R. R.; Blake, P.; Anisimova, S.; Novoselov, K. S.; Geim, A. K. Spectroscopic Ellipsometry of Graphene and an Exciton-Shifted Van Hove Peak in Absorption. *Phys. Rev. B* **2010**, *81*, 155413.
95. Nair, R. R.; Blake, P.; Grigorenko, A. N.; Novoselov, K. S.; Booth, T. J.; Stauber, T.; Peres, N. M. R.; Geim, A. K. Fine Structure Constant Defines Visual Transparency of Graphene. *Science* **2008**, *320*, 1308–1308.
96. Casiraghi, C.; Hartschuh, A.; Lidorikis, E.; Qian, H.; Harutyunyan, H.; Gokus, T.; Novoselov, K. S.; Ferrari, A. C. Rayleigh Imaging of Graphene and Graphene Layers. *Nano Lett.* **2007**, *7*, 2711–2717.
97. Meyer, J. C.; Geim, A. K.; Katsnelson, M. I.; Novoselov, K. S.; Booth, T. J.; Roth, S. The Structure of Suspended Graphene Sheets. *Nature* **2007**, *446*, 60–63.
98. Meyer, J. C.; Geim, A. K.; Katsnelson, M. I.; Novoselov, K. S.; Obergfell, D.; Roth, S.; Girit, C.; Zettl, A. On the Roughness of Single- and Bi-Layer Graphene Membranes. *Solid State Commun.* **2007**, *143*, 101–109.
99. Ferrari, A. C.; Meyer, J. C.; Scardaci, V.; Casiraghi, C.; Lazzeri, M.; Mauri, F.; Piscanec, S.; Jiang, D.; Novoselov, K. S.; Roth, S.; *et al.* Raman Spectrum of Graphene and Graphene layers. *Phys. Rev. Lett.* **2006**, *97*, 187401.
100. Khan, U.; O'Neill, A.; Lotya, M.; De, S.; Coleman, J. N. High-Concentration Solvent Exfoliation of Graphene. *Small* **2010**, *6*, 864–871.
101. Hansen, C. M. *Hansen Solubility Parameters: A User's Handbook*; CRC Press Inc.: Boca Raton, FL, 2007.
102. Bergin, S. D.; Nicolosi, V.; Streich, P. V.; Giordani, S.; Sun, Z.; Windle, A. H.; Ryan, P.; Niraj, N. P. P.; Wang, Z.-T.; Carpenter, L.; *et al.* Towards Solutions of Single-Walled Carbon Nanotubes in Common Solvents. *Adv. Mater.* **2008**, *20*, 1876–1881.
103. Lotya, M.; King, P. J.; Khan, U.; De, S.; Coleman, J. N. High-Concentration, Surfactant-Stabilized Graphene Dispersions. *ACS Nano* **2010**, *4*, 3155–3162.
104. Williams, J. W.; Van Holde, K. E.; Baldwin, R. L.; Fujita, H. The Theory of Sedimentation Analysis. *Chem. Rev.* **1958**, *58*, 715–806.
105. Schuck, P. Size-Distribution Analysis of Macromolecules by Sedimentation Velocity Ultracentrifugation and Lamm Equation Modeling. *Biophys. J.* **2000**, *78*, 1606–1619.
106. Svedberg, T.; Pedersen, K. O. *The Ultracentrifuge*; Oxford University Press: London, 1940.
107. Ferrari, A. C.; Robertson, J. Interpretation of Raman Spectra of Disordered and Amorphous Carbon. *Phys. Rev. B* **2000**, *61*, 14095–14107.
108. Tuinstra, F.; Koenig, J. L. Raman Spectrum of Graphite. *J. Chem. Phys.* **1970**, *53*, 1126–1130.
109. Piscanec, S.; Lazzeri, M.; Mauri, F.; Ferrari, A. C.; Robertson, J. Kohn Anomalies and Electron-Phonon Interactions in Graphite. *Phys. Rev. Lett.* **2004**, *93*, 185503.
110. Casiraghi, C.; Hartschuh, A.; Qian, H.; Piscanec, S.; Georgi, C.; Fasoli, A.; Novoselov, K. S.; Basko, D. M.; Ferrari, A. C. Raman Spectroscopy of Graphene Edges. *Nano Lett.* **2009**, *9*, 1433–1441.
111. Ferrari, A. C.; Robertson, J. Resonant Raman Spectroscopy of Disordered, Amorphous, and Diamondlike Carbon. *Phys. Rev. B* **2001**, *64*, 075414.
112. Cancado, L. G.; Jorio, A.; Ferreira, E. H. M.; Stavale, F.; Achete, C. A.; Capaz, R. B.; Moutinho, M. V. O.; Lombardo, A.; Kulmala, T. S.; Ferrari, A. C. Quantifying Defects in Graphene via Raman Spectroscopy at Different Excitation Energies. *Nano Lett.* **2011**, *11*, 3190–3196.
113. Ferrari, A. C.; Rodil, S. E.; Robertson, J. Resonant Raman Spectra of Amorphous Carbon Nitrides: the G Peak Dispersion. *Diam. Relat. Mater.* **2003**, *12*, 905–910.
114. Ferrari, A. C. Diamond-like Carbon for Magnetic Storage Disks. *Surf. Coat. Technol.* **2004**, *180–181*, 190–206.
115. Basko, D. M.; Piscanec, S.; Ferrari, A. C. Electron-Electron Interactions and Doping Dependence of the Two-Phonon Raman Intensity in Graphene. *Phys. Rev. B* **2009**, *80*, 165413.
116. Das, A.; Pisana, S.; Chakraborty, B.; Piscanec, S.; Saha, S. K.; Waghmare, U. V.; Novoselov, K. S.; Krishnamurthy, H. R.; Geim, A. K.; Ferrari, A. C.; *et al.* Monitoring Dopants by Raman Scattering in an Electrochemically Top-Gated Graphene Transistor. *Nat. Nanotechnol.* **2008**, *3*, 210–215.
117. Pisana, S.; Lazzeri, M.; Casiraghi, C.; Novoselov, K. S.; Geim, A. K.; Ferrari, A. C.; Mauri, F. Breakdown of the Adiabatic

- Born Oppenheimer Approximation in Graphene. *Nat. Mater.* **2007**, *6*, 198–201.
118. Coleman, J. N.; Lotya, M.; O'Neill, A.; Bergin, S. D.; King, P. J.; Khan, U.; Young, K.; Gaucher, A.; De, S.; Smith, R. J.; *et al.* Two-Dimensional Nanosheets Produced by Liquid Exfoliation of Layered Materials. *Science* **2011**, *331*, 568–571.
 119. Young, T. An Essay on the Cohesion of Fluids. *Philos. Trans. R. Soc. London* **1805**, *95*, 65–87.
 120. Shafrin, E. G.; Zisman, W. A. Critical Surface Tension for Spreading on a Liquid Substrate. *J. Phys. Chem.* **1967**, *71*, 1309–1316.
 121. Thomas, R. R.; Kaufman, F. B.; Kirleis, J. T.; Belsky, R. A. Wettability of Polished Silicon Oxide Surfaces. *J. Electrochem. Soc.* **1996**, *143*, 643–648.
 122. Glendinning, W. B.; Helbert, J. N. *Handbook of VLSI Microlithography: Principles, Technology, and Applications*; Noyes: Saddle River, NJ, 1991.
 123. Ghatee, M. H.; Pakdel, L. Surface Tension Regularity of Non-Polar, Polar, and Weak Electrolyte Liquid Hydrocarbons. *Fluid Phase Equilib.* **2005**, *234*, 101–107.
 124. Marmur, A. Wetting on Hydrophobic Rough Surfaces: To Be Heterogeneous or Not To Be? *Langmuir* **2003**, *19*, 8343–8348.
 125. Duineveld, P. C. The Stability of Ink-Jet Printed Lines of Liquid with Zero Receding Contact Angle on a Homogeneous Substrate. *J. Fluid Mech.* **2003**, *477*, 175–200.
 126. Kaye, B. H. In *Powder Mixing*; Chapman & Hall: London, 1997.
 127. Gamerith, S.; Klug, A.; Scheiber, H.; Scherf, U.; Moderegger, E.; List, E. J. W. Direct Ink-Jet Printing of Ag-Cu Nanoparticle and Ag-Precursor Based Electrodes for OFET Applications. *Adv. Func. Mater.* **2007**, *17*, 3111–3118.
 128. Smits, F. M. Measurement of Sheet Resistivities with the Four-Point Probe. *Bell Syst. Tech. J.* **1958**, *37*, 711–718.
 129. Hu, L.; Hecht, D. S.; Gruner, G. Percolation in Transparent and Conducting Carbon Nanotube Networks. *Nano Lett.* **2004**, *4*, 2513–2517.
 130. Geng, H. Z.; Kim, K. K.; So, K. P.; Lee, Y. S.; Chang, Y.; Lee, Y. H. Effect of Acid Treatment on Carbon Nanotube-Based Flexible Transparent Conducting Films. *J. Am. Chem. Soc.* **2007**, *129*, 7758–7759.
 131. De, S.; King, P. J.; Lyons, P. E.; Khan, U.; Coleman, J. N. Size Effects and the Problem with Percolation in Nanostructured Transparent Conductors. *ACS Nano* **2010**, *4*, 7064–7072.
 132. De, S.; King, P. J.; Lotya, M.; O'Neill, A.; Doherty, E. M.; Hernandez, Y.; Duesberg, G. S.; Coleman, J. N. Flexible, Transparent, Conducting Films of Randomly Stacked Graphene from Surfactant-Stabilized, Oxide-Free Graphene Dispersions. *Small* **2009**, *6*, 458–464.
 133. Kirkpatrick, S. Percolation and Conduction. *Rev. Mod. Phys.* **1973**, *45*, 574.
 134. Stauffer, D.; Aharony, A. In *Introduction to Percolation Theory*; Taylor&Francis: London, 1985.
 135. Kogut, P. M.; Straley, J. P. Distribution-Induced Non-Universality of the Percolation Conductivity Exponents. *J. Phys. C: Solid State* **1979**, *12*, 2151–2159.
 136. Johnner, N.; Grimaldi, C.; Balberg, I.; Ryser, P. Transport Exponent in a Three-Dimensional Continuum Tunneling-Percolation Model. *Phys. Rev. B* **2008**, *77*, 174204.
 137. Doherty, E. M.; De, S.; Lyons, P. E.; Shmeliov, A.; Nirmalraj, P. N.; Scardaci, V.; Joimel, J.; Blau, W. J.; Boland, J. J.; Coleman, J. N. The Spatial Uniformity and Electromechanical Stability of Transparent, Conductive Films of Single Walled Nanotubes. *Carbon* **2009**, *47*, 2466–2473.
 138. <http://www.epson.com/cgi-bin/Store/Landing/InkTech-Cartridges.jsp> access on April 2011.
 139. Kuzmenko, A. B.; van Heumen, E.; Carbone, F.; van der Marel, D. Universal Optical Conductance of Graphite. *Phys. Rev. Lett.* **2008**, *100*, 117401.
 140. Ong, B. S.; Wu, Y.; Liu, P.; Gardner, S. High-Performance Semiconducting Polythiophenes for Organic Thin-Film Transistors. *J. Am. Chem. Soc.* **2004**, *126*, 3378–3379.
 141. Arias, A. C.; Ready, S. E.; Lujan, R.; Wong, W. S.; Paul, K. E.; Salleo, A.; Chabinyc, M. L.; Apte, R.; Street, R. A.; Wu, Y.; *et al.* All Jet-Printed Polymer Thin-Film Transistor Active-Matrix Backplanes. *Appl. Phys. Lett.* **2004**, *85*, 3304–3306.
 142. Wu, Y.; Liu, P.; Ong, B. S.; Srikumar, T.; Zhao, N.; Botton, G.; Zhu, S. Controlled Orientation of Liquid-Crystalline Polythiophene Semiconductors for High-Performance Organic Thin-Film Transistors. *Appl. Phys. Lett.* **2005**, *86*, 142102.
 143. Kaneto, K.; Yano, M.; Shibao, M.; Morita, T.; Takashima, W. Ambipolar Field-Effect Transistors Based on Poly(3-hexylthiophene)/Fullerene Derivative Bilayer Films. *Jpn. J. Appl. Phys.* **2007**, *46*, 1736–1738.
 144. Morita, T.; Singh, V.; Oku, S.; Nagamatsu, S.; Takashima, W.; Hayase, S.; Kaneto, K. Ambipolar Transport in Bilayer Organic Field-Effect Transistor Based on Poly(3-hexylthiophene) and Fullerene Derivatives. *Jpn. J. Appl. Phys.* **2010**, *49*, 04161–04166.
 145. Oh, J. H.; Lee, H. W.; Mannsfeld, S.; Stoltenberg, R. M.; Jung, E.; Jin, Y. W.; Kim, J. M.; Yoo, J.-B.; Bao, Z. Solution-Processed, High-Performance N-channel Organic Micro-wire Transistors. *Proc. Natl. Acad. Sci. U. S. A.* **2009**, *106*, 6065–6070.
 146. Siringhaus, H.; Tessler, N.; Friend, R. H. Integrated Optoelectronic Devices Based on Conjugated Polymers. *Science* **1998**, *280*, 1741–1744.
 147. Song, Y. J.; Lee, J. U.; Jo, W. H. Multi-Walled Carbon Nanotubes Covalently Attached with Poly(3-hexylthiophene) for Enhancement of Field-Effect Mobility of Poly(3-hexylthiophene)/Multi-Walled Carbon Nanotube Composites. *Carbon* **2010**, *48*, 389–395.
 148. Whiting, G. L.; Arias, A. C. Chemically Modified Ink-jet Printed Silver Electrodes for Organic Field-Effect Transistors. *Appl. Phys. Lett.* **2009**, *95*, 253302–253303.
 149. Klauk, H. In *Organic Electronics*; Wiley-VCH: Weinheim, 2006; Chapter 4.
 150. Chason, M.; Brazis, P. W.; Zhang, J.; Kalyanasundaram, K.; Gamota, D. R. Printed Organic Semiconducting Devices. *Proc. IEEE* **2005**, *93*, 1348–1356.
 151. Kawase, T.; Moriya, S.; Newsome, C. J.; Shimoda, T. Inkjet Printing of Polymeric Field-Effect Transistors and Its Applications. *Jpn. J. Appl. Phys.* **2005**, *44*, 3649–3658.
 152. Parmer, J. E.; Mayer, A. C.; Hardin, B. E.; Scully, S. R.; McGehee, M. D.; Heeney, M.; McCulloch, I. Organic Bulk Heterojunction Solar Cells using Poly(2,5-bis(3-tetradecylthiophen-2-yl)thieno[3,2-b]thiophene). *Appl. Phys. Lett.* **2008**, *92*, 113309–113303.
 153. Padday, J. F. The Profiles of Axially Symmetric Menisci. *Philos. Trans. R. Soc. London A* **1971**, *269*, 265–293.